THE GEOLOGICAL SOCIETY OF AMERICA®

Low-grade retrogression of a high-temperature metamorphic core complex: Naxos, Cyclades, Greece

Shuyun Cao[1,2,†], Franz Neubauer[1], Manfred Bernroider[1], Johann Genser[1], Junlai Liu[3], and Gertrude Friedl[1]

[1]*Department of Geography and Geology, University of Salzburg, Hellbrunnerstrasse 34, A-5020 Salzburg, Austria*

[2]*State Key Laboratory of Geological Processes and Mineral Resources, School of Earth Sciences, China University of Geosciences, Wuhan 430074, China*

[3]*State Key Laboratory of Geological Processes and Mineral Resources, China University of Geosciences, Beijing 100083, China*

ABSTRACT

Retrogressive deformation and metamorphism are often reported from the main low-angle shear zones and detachments of metamorphic core complexes, but their importance is not sufficiently emphasized for the footwall interior. In order to contribute to a better understanding of exhumation-related retrogression processes within and at the top of metamorphic core complexes, an integrated detailed microstructural, textural, $^{40}Ar/^{39}Ar$ geochronological, and thermobarometric study on the Naxos metamorphic core complex within the Aegean Sea is presented that provides a new perspective on low-grade retrogression during exhumation through shallow ductile levels. We found variable retrogressive deformation within the Naxos metamorphic core complex, which even pervasively affected significant portions of the migmatite-grade metamorphic core and remnant high-pressure areas of the metamorphic core complex, where retrogression led to pervasive formation of new fabrics within greenschist-facies metamorphic conditions during brittle-ductile transition. Within a continuum of retrogression, $^{40}Ar/^{39}Ar$ white mica dating allowed us to deduce three retrogressive ages at 16.52 ± 0.39 Ma (within the Naxos metamorphic core complex), 12.6 ± 0.28 Ma (Moutsounas detachment shear zone on the eastern boundary of the metamorphic core complex), and 10.43 ± 0.44 Ma to 8.40 ± 0.76 Ma (last ductile activity along the Naxos-Paros shear zone to the north of the metamorphic core complex). A further stage of retrogression at 12–11 Ma occurred along distinct low-angle normal faults within the middle Miocene Naxos Granite. Retrogressive microstructures, low-temperature calcite fabrics in marbles, and chloritization in metapelites (at temperatures of ~350–130 °C) in the metamorphic core complex core resulted mainly from late-stage E-W shortening and folding. Late-stage flow of hydrous fluids resulted in resetting of fabrics and enhancement of ductile deformation. The middle–late Miocene retrogression events are also reflected by a similarly aged tectonic collapse basin in the hanging-wall unit above the detachment. The wide temporal range of retrogression within the Naxos metamorphic core complex coincides in age with retrogressive deformation within other metamorphic core complexes of the Aegean Sea. We interpret the long temporal range of retrogression to reflect outward, southwestward retreat of the subduction and sequential activation of major detachment zones.

INTRODUCTION

In tectonic reconstructions, the recognition of exhumed crust is critically important because such rocks provide information on the tectono-thermal history of the crust. This is particularly the case for metamorphic core complexes with plastically deformed rocks exhumed from middle- to lower-crustal levels to the surface (e.g., Whitney et al., 2013, and references therein; Platt et al., 2015, and references therein). Many details are known concerning the exhumation history and structures related to exhumation, juxtaposing the typically high-temperature metamorphic core complex against older metamorphic and sedimentary upper-plate rocks. Deformation stages within metamorphic core complexes are the result of various superimposed processes, which range from initial viscous deformation to brittle deformation and also include syn-kinematic fluid flow (e.g., Lister and Davis, 1989; Verdel et al., 2007; Kargaranbafghi et al., 2012). Exhumation can channelize the flow of hydrous fluids and limit pervasive retrogression of metamorphic complexes along the upper margins, particularly close to the brittle-ductile boundary (e.g., Siebenaller et al., 2013; Whitney et al., 2013; Gébelin et al., 2014; Methner et al., 2015, and references therein).

Low-temperature retrogressive deformation and metamorphism of high-grade metamorphic fabrics are often reported from detachments of metamorphic core complexes (e.g., Mehl et al., 2007; Harigane et al., 2008; Hetzel et al., 2013; Whitney et al., 2013). The detachment fault is characterized by retrogressive shear fabrics and forms under decreasing temperature-pressure conditions from usually ductile deformation within amphibolite-facies conditions (>500 °C) through the brittle-ductile transition (250–400 °C) to purely brittle conditions (e.g., Whitney et al., 2013). This is expressed by chloritization of mafic minerals, sericitization of feldspars, and formation of chlorite breccia at the top by pervasive fluid flow (e.g., Cathelineau and Nieva, 1985; Cathelineau, 1988; Kirschner et al., 1996; Dunlap, 1997; Reddy and Potts, 1999). In some metamorphic core complexes, low-grade retrogression may also occur in the interior during exhumation, and several studies have reported local retrogressive shear zones (e.g., Urai et al., 1990; Urai and Feenstra, 2001; Parra et al., 2002). Although previous workers have already noted this retrograde deformation in the footwall of metamorphic core complexes, they have not sufficiently emphasized its importance. The importance of widespread retrogression in the interior of metamorphic core complexes and its temporal and structural relationships to detachments are the focus of this study.

In this study, based on structural field work, we completed detailed microstructural and textural investigations, thermobarometric calculations, and $^{40}Ar/^{39}Ar$ white mica dating of retrogressive fabrics to reveal the significance of low-grade retrogression of high- and medium-grade metamorphic and granitic rocks. These results,

[†]shuyun.cao@sbg.ac.at

GSA Bulletin; doi: 10.1130/B31502.1; 13 figures; 1 table; Data Repository item 2016294.

combined with previous studies, provide new insights into the regional retrogression associated with ductile to ductile-brittle deformation and cooling of the Naxos metamorphic core complex. The new data also allow fresh insights into the mode and history of tectonic extension in the Aegean region during Neogene times, and the methodology could possibly be transferred to other metamorphic core complexes.

GEOLOGY OF THE SOUTHERN AEGEAN SEA REGION

One of the most striking features within the south-central Aegean region is the sequential north to south formation of numerous metamorphic core complexes along the North Cycladic (e.g., Andros, Tinos, Mykonos, and Ikaria), Central Cycladic (including the Naxos-Paros detachment), and West Cycladic (Sifnos, Serifos, Kea) detachments (Fig. 1; Jolivet et al., 2010; Grasemann et al., 2012). The development of these metamorphic core complexes has been linked to N-S extension of the Aegean lithosphere in the backarc domain of the Hellenic subduction zone (Lister et al., 1984; Jolivet et al., 2003; Krohe et al., 2010, and references therein) in the early Neogene (ca. 23 Ma; Gautier et al., 1993; Tirel et al., 2008; Ring et al., 2007, 2010). Extension was and is triggered by the southward retreat of the African slab (e.g., Le Pichon and Angelier, 1981; Jolivet and Faccenna, 2000; Huet et al., 2009, 2011; Jolivet et al., 2010; Ring et al., 2010; Grasemann et al., 2012).

The Attic-Cycladic Belt includes two units, the lower Cycladic basement unit (mainly granitoids, and/or migmatite, and gneiss overlain by a thin layer of mica schist) and the middle Cycladic Blueschist unit (e.g., Ring et al., 2001, 2007, 2010; Huet et al., 2009, 2011; Royden and Papanikolaou, 2011; Jolivet et al., 2013). They form the footwall units within the metamorphic core complexes. The upper plate contains nearly unmetamorphosed ophiolites and Miocene sedimentary formations (for details, see following). Extension associated with exhumation of the Attic-Cycladic Belt resulted

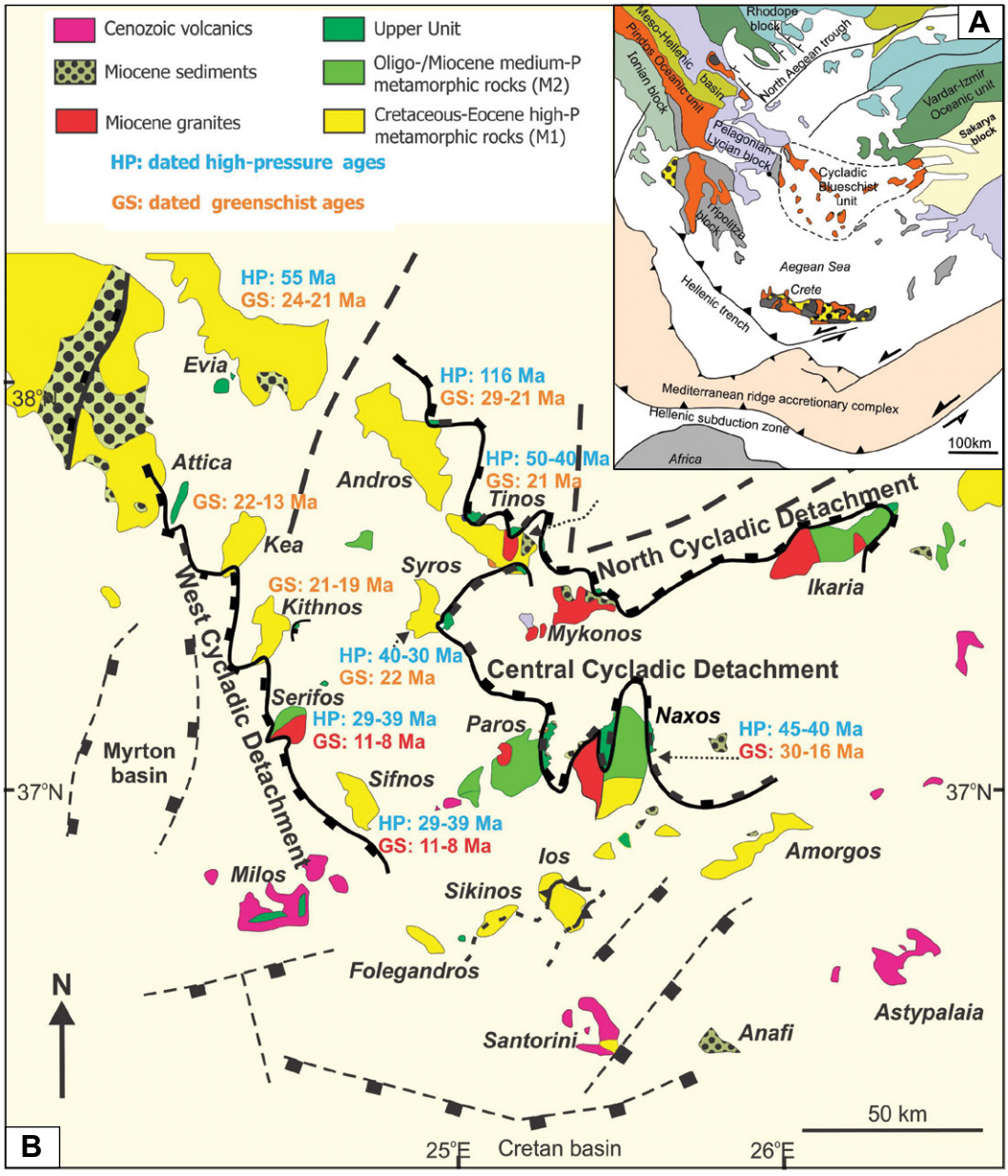

Figure 1. (A) Simplified tectonic map of the Aegean region showing the main tectonic zones above the Hellenic subduction zone (modified after Jolivet et al., 2010). (B) Simplified geological map of Cyclades and ages of high-pressure metamorphism and retrogression, mainly based on results of $^{40}Ar/^{39}Ar$ dating. Data sources: Wijbrans and Mcdougall (1986, 1988); Wijbrans et al. (1990); Bröcker et al. (1993, 2004, 2013); Huet et al. (2015); Cossette et al. (2015).

in crustal thinning, tectonic unroofing, high heat flow and, in some islands, emplacement of Miocene magmatic arc–related I- and S-type granites within the metamorphic core complexes (e.g., Pe-Piper et al., 1997; Bolhar et al., 2010; Kruckenberg et al., 2011) and finally in surface exposure of the lower Cycladic basement unit and the middle Cycladic Blueschist unit (Ring et al., 2003). Tectonic unroofing continued in places until latest Miocene times, associated with a gradient in retrogression of the high-pressure–low-temperature (HP-LT) parageneses (Parra et al., 2002), as recorded by apatite fission-track cooling ages (e.g., Hejl et al., 2002; Brichau et al., 2010). The Alpine metamorphic history of Attic-Cycladic Belt includes Meso-Hellenic high-pressure metamorphism (M1) mainly at ca. 45 Ma (and ages as old as 116 Ma; Huet et al., 2015) and Neo-Hellenic Barrovian-type metamorphism (M2) at greenschist facies to local amphibolite facies (on Naxos) overprinting high-pressure rocks. M1 metamorphism formed due to crustal thickening during Hellenic subduction in the Cyclades (e.g., Jacobshagen, 1986). The timing of the M2 metamorphic overprint is largely constrained between 20 and 12 Ma (e.g., Altherr et al., 1982; Andriessen et al., 1987; Wijbrans and McDougall, 1988; Okrusch and Bröcker, 1990; Avigad, 1998; Keay et al., 2001; Tomaschek et al., 2003; Kumerics et al., 2005). Ages of retrogression after M1 and M2 metamorphism scatter over a wide range between 30 and 8 Ma (Fig. 1B).

The upper units above the detachments consist of the weakly to nonmetamorphic composite Cycladic ophiolite nappe and latest Oligocene to Pliocene sediments (Böger, 1983; Lister et al., 1984; Avigad and Garfunkel, 1991; Lee and Lister, 1992) interpreted as infill of collapse-type basins resting on the upper unit (e.g., Sanchez-Gomez et al., 2002; Bargnesi et al., 2013).

GEOLOGY AND EXHUMATION HISTORY OF THE NAXOS METAMORPHIC CORE COMPLEX

Since its recognition as a metamorphic core complex (Lister et al., 1984), extensive research on the classic Naxos metamorphic core complex has provided a wealth of information on its structure, thermal and geomorphologic evolution, and tectonic implications (e.g., Jansen and Schuiling, 1976; Duchêne et al., 2006; Schenk et al., 2007; Vanderhaeghe et al., 2007; Seward et al., 2009; Kruckenberg et al., 2011; Cao et al., 2013a; Siebenaller et al., 2013). Here, we focus on a summary of the main points needed for the purpose of this study.

Structure of Naxos

The classic Naxos metamorphic core complex lies in the Cyclades in the western Aegean Sea and is associated with the Naxos-Paros ductile low-angle fault (e.g., Lister et al., 1984; Gautier et al., 1993) along the northern margins of Naxos and Paros, which is part of the Central Cycladic detachment system (Fig. 1; Jolivet et al., 2010). The main structure of the Naxos metamorphic core complex is a migmatite-cored gneiss dome with marbles, calc-schists, phengite-schists, orthogneisses, migmatites, and amphibolites, and this is structurally overlain by a low-angle normal fault in the east and a steep strike-slip–type fault zone in the west (Fig. 2). The western part of Naxos exposes the Miocene Naxos Granite (e.g., Pe-Piper et al., 1997; Koukouvelas and Kokkalas, 2003). The hanging-wall unit of the Naxos metamorphic core complex and Naxos Granite consists of remnants of unmetamorphosed Mesozoic ophiolites and overlying Miocene and Pliocene sedimentary rocks (Kuhlemann et al., 2004), which form a synform between the Naxos metamorphic core complex and the Naxos Granite.

Metamorphic Stages and Subsequent Cooling

Two main successive Alpine metamorphic events affected the metamorphic zoning within the Naxos metamorphic core complex (e.g., Andriessen et al., 1979; Urai et al., 1990; Keay et al., 2001). The earlier HP-LT Eocene metamorphism (M1) phase is recorded by relics of blueschist-facies assemblages preserved in metamorphic rocks in the southern part of the island of Naxos (~12 kbar, 470 °C, ~13 °C/km; Wijbrans and McDougall, 1986; Avigad and Garfunkel, 1991; Avigad, 1998). No field gradient is known because of overprint of the M1 phase by M2 metamorphism in central and northern Naxos. The $^{40}Ar/^{39}Ar$ white mica ages of ca. 45 ± 5 Ma document an Eocene age for blueschist metamorphism on Naxos (Andriessen et al., 1979; Wijbrans and McDougall, 1986, 1988). Martin et al. (2006) presented evidence for M1 high-pressure metamorphic conditions within the high-grade rocks affected by M2 metamorphism.

Based on NE-SW–trending mineral zones, which delineate a metamorphic dome (Fig. 2A), M2 metamorphism grades from greenschist-facies conditions in SE Naxos to amphibolite-facies conditions in northern central Naxos and reached conditions conducive to migmatization in the dome core (650–700 °C, 6–7 kbar; Jansen and Schuiling, 1976; Buick and Holland, 1989). M2 metamorphism was accompanied by intense foliation development and isoclinal folding (D1; Urai et al., 1990; Vanderhaeghe et al., 2007; Kruckenberg et al., 2011).

After initial attempts with K-Ar ages giving results of ca. 15 Ma (hornblende) to ca. 11 Ma (mica; Jansen and Schuiling, 1976; Jansen, 1977), the timing of peak Barrovian-type M2 metamorphism is dated now by Rb/Sr mica and garnet ages (Duchêne et al., 2006) and U-Pb zircon rim ages to range from 19 to 14 Ma (Keay, 1998; Keay et al., 2001; Martin et al., 2006, 2008). An age of 20–25 Ma for the M2 greenschist-facies retrogression has been proposed (Andriessen et al., 1979; Andriessen, 1991), whereas Wijbrans and McDougall (1988) reported $^{40}Ar/^{39}Ar$ white mica ages of 27 and 19.9 Ma, which they interpreted to possibly relate to partial retrogression after M1 metamorphism. Duchêne et al. (2006) dated recrystallized phengitic white mica in a sample from zone III (Fig. 2) and interpreted the 29.3 Ma age to represent the retrogressive evolution from peak M1 to M2 recrystallization, which is dated at 22.7–19.8 Ma by K/Ar, $^{40}Ar/^{39}Ar$, and Rb/Sr on muscovite.

Zircon fission-track ages range from 25.2 ± 3.8 Ma to 9.3 ± 2.8 Ma (with youngest ages within the migmatite dome), and apatite fission-track ages range from 11.2 ± 1.6 MA to 8.2 ± 1.2 Ma (Seward et al., 2009). Apatite fission-track ages, however, are progressively younger from south to north, varying from 12.9 to 9.0 Ma (Seward et al., 2009). Brichau et al. (2006) presented zircon fission-track ages ranging between 11.8 ± 0.8 Ma and 9.7 ± 0.8 Ma and apatite fission-track ages from 11.2 ± 1.6 Ma to 8.2 ± 1.2 Ma. A single (U-Th)/He apatite age of 10.9 Ma is available from the migmatite core of the Naxos metamorphic core complex (Vermeesch et al., 2007).

Recently, Siebenaller et al. (2013) studied fluids from quartz veins, mainly from the southern part of the M2 migmatite core. They distinguished immiscible CO_2-rich fluid and a high-salinity brine generated by metamorphic reactions and magma crystallization, respectively. Fluids were initially trapped at 625 °C and 400 MPa and then remobilized during ductile deformation at ~350 °C and 140 MPa. Brittle microcracks contain aqueous meteoric fluids trapped at 250 °C and 80 MPa. This peculiar retrograde pressure-temperature (*P-T*) pathway implies that the brittle-ductile transition zone separated two fluid reservoirs, namely (1) the ductile crust, into which fluids originating from crystallizing magmas and fluids in equilibrium with metamorphic rocks circulated at a geothermal gradient of 30 °C/km at lithostatic pressure, and (2) the brittle upper crust, through which

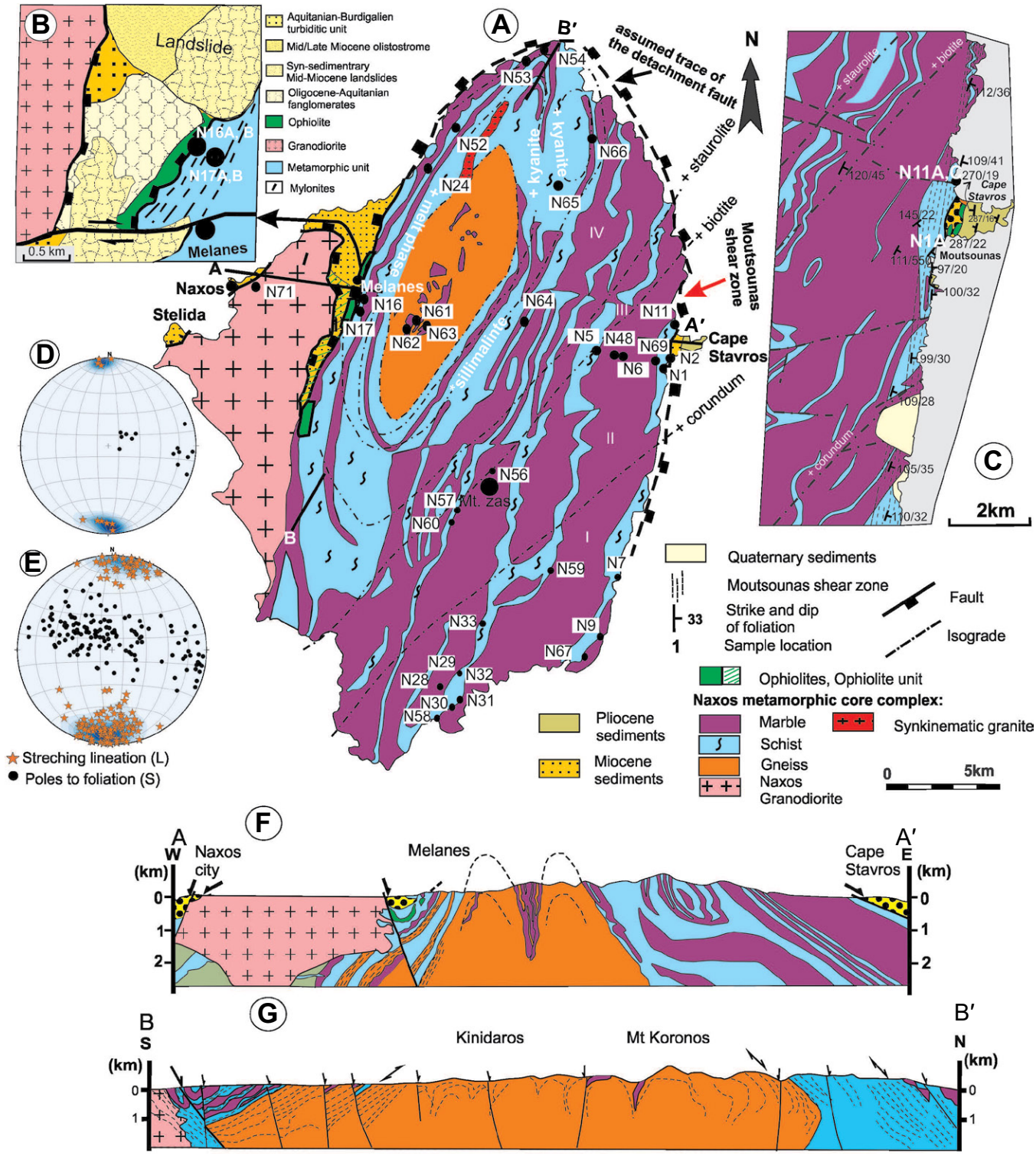

Figure 2. (A) Geological map of the Naxos metamorphic core complex in the Cyclades Islands, Greece, showing lithologies, metamorphic isograds, and faults with arrows for kinematics after John and Howard (1995), Keay et al. (2001), and Koukouvelas and Kokkalas (2003), and sample locations. (B) Detailed geological map of the Melanes area in the northwestern central sectors of Naxos island with sample locations (modified after Jansen, 1977; Vanderhaeghe et al., 2007). (C) Detail of the eastern sectors of Naxos Island with sample locations (modified after Jansen, 1977). (D) Lower-hemisphere, equal-area stereoplot of foliation planes and stretching lineation of the Melanes shear zone. (E) Lower-hemisphere, equal-area stereoplot of foliation planes and stretching lineation of the Naxos metamorphic core complex. (F) E-W cross section across Naxos showing the general structure of the Naxos metamorphic core complex dome in the east and the Naxos Granite dome in the west (Jansen, 1973; Vanderhaeghe, 2004). (G) N-S cross section across Naxos (modified after Jansen, 1973; Vanderhaeghe, 2004).

meteoric fluids percolated along a high geothermal gradient of 55 °C/km at hydrostatic pressure (Siebenaller et al., 2013).

Miocene Plutonism and Cooling

The I-type Naxos Granite, with mostly granite and subordinate granodiorite mainly at margins, is now in tectonic contact with the Miocene clastic succession in northern Naxos. The Naxos Granite body was emplaced at ca. 12–14 Ma according to U/Pb dating of zircons (e.g., Henjes-Kunst et al., 1988; Pe-Piper et al., 1997; Keay et al., 2001; Bolhar et al., 2010). Rapid cooling of the batholith is indicated by the ca. 12.5 Ma $^{40}Ar/^{39}Ar$ ages from various minerals (Wijbrans and McDougall, 1988), a K-Ar biotite age of ca. 10 Ma (Pe-Piper et al., 1997), and pseudotachylyte formation at ca. 10 Ma (Andriessen et al., 1979). Zircon and apatite fission-track ages of the Naxos Granite range from 13.7 ± 2.2 Ma to 12.2 ± 1.4 Ma and 12.9 ± 4.4 to 9.0 ± 2.6 Ma, respectively (Altherr et al., 1982; Hejl et al., 2003; Brichau et al., 2006; Seward et al., 2009), which is coeval with top-to-the-north, low-angle normal faulting. The (U-Th)/He ages range from 10.4 ± 0.4 Ma to 9.2 ± 0.3 and 10.7 ± 1.0 Ma to 8.9 ± 0.6 Ma for zircon and apatite, respectively (Brichau et al., 2006). Together, the mentioned geochronological data from the Naxos metamorphic core complex and Naxos Granite were used to determine slip rates of 6.4 (+6.8/–2.2) mm/yr to 13.2 (+9.4/–4.5) mm/yr over the temperature range from ~300 °C to ~40 °C for the brittle phase of northward slip along the detachment (Brichau et al., 2010).

MAIN RETROGRESSIVE DEFORMATION STRUCTURES WITHIN THE NAXOS METAMORPHIC CORE COMPLEX

In this section, we describe the retrogressive deformation structures within the Naxos metamorphic core complex from field observations and macroscopic structural analysis. All microstructural details from samples in the interior and boundary shear zones of the Naxos metamorphic core complex and the Naxos Granite are compiled in Table 1 and the section titled "Retrogressive Microfabrics." In the field, zones of retrogression are characterized by the presence of quartz and calcite veins and variable chloritization of otherwise chlorite-free lithologies.

Mineral deformation features and rock microstructures were characterized with special reference to feldspar, quartz, white mica, biotite, calcite, and chlorite. Texture measurements were performed on quartz and calcite (section on "Crystallographic Preferred Orientations Related to Retrogressive Fabrics"). The deformation and metamorphism conditions were estimated using the microstructure, texture, and mineral thermometry (section on "Conditions of Metamorphism during Retrogression") followed by white mica $^{40}Ar/^{39}Ar$ dating results ("White Mica $^{40}Ar/^{39}Ar$ Dating" section).

Structures of the Internal Naxos Metamorphic Core Complex

Although high-pressure mineral relics are preserved in the M1-dominated zone, our detailed ductile structural analysis, particularly of calcite marbles and phyllitic rocks, reveals that there is no structural difference between these two M1- and M2-dominated domains. Both units are pervasively affected by retrogression and show similarly oriented ductile fabrics, including the NNE-trending stretching lineation. All rocks have a pervasive foliation (S) and a similarly oriented NNE- or SSW-plunging stretching lineation (Fig. 2E). Bookshelf domino-type structures (Fig. 3A) indicate top-to-the-NNE transport. Boudinage parallel to the NNE-SSW–trending stretching lineation of rheologically stiff layers within calcite marbles is a common phenomenon (Fig. 3B). In the center of the migmatite dome, S-type granites intruded, as well as aplite and granitic dikes. These, as well as the penetrative foliation, are folded around N-S–trending fold axes (Figs. 3C and 3D) and therefore postdate peak conditions of S and L formation. The folded aplitic dikes and country rocks often reveal a steep approximately N-S–striking axial plane foliation (Fig. 3E), which is less intense in the south.

Mostly subvertical granite dikes are variably deformed and folded (see previous) or postdate the penetrative foliation (Fig. 3F). In the latter case, these dikes often strike N-S and bear a weak subvertical foliation similar in strike to the axial plane foliation. Subvertical, mostly E-W–striking, calcite-filled veinlets and extensional veins filled with coarse epitaxial (rim) and isometric calcite crystals occur within the marble sometimes (Figs. 3G–3I). They document approximately N-S stretching and fluid flow during late stages of the exhumation of the Naxos metamorphic core complex.

Western Boundary Shear Zone at Melanes

In the surroundings of Melanes, at the western border of the Naxos metamorphic core complex, a subvertical belt of fine-grained N-S–striking mylonites is exposed (here termed the Melanes shear zone; Figs. 2B, 2D, and 4), and these form the western, structurally upper boundary of the Naxos metamorphic core complex, against which the unmetamorphic ophiolites are juxtaposed to the west (Fig. 2B). The Melanes shear zone is characterized by mylonitic rocks (amphibolite, paragneiss, and marble) with a gently W-dipping foliation and a penetrative subhorizontal N-S–trending stretching lineation. The microboudins and late extensional veins (quartz, chlorite) and microfaults are filled with chlorite (Figs. 4A and 4B).

Naxos Granite

At the southern end, the contact between the hornblende-biotite granite and schists in the Naxos metamorphic core complex is exposed (Fig. 4C), with the foliation of the country rocks predating granodiorite intrusion. There, the granite and mafic enclaves exhibit a magmatic and/or high-temperature N-S–striking solid-state foliation and a stretching lineation defined by elongated feldspars, amphibole, and biotite (Figs. 4D–4G). The stretching lineation plunges moderately to the south. Internally, undeformed granite dikes postdate the foliation. Along its northern and eastern margin, the granodiorite shows abundant signs of retrogression, mainly chloritization along shear zones and faults and chloritized protocataclasites, with some ductile overprint during retrogression at the eastern margin (Figs. 4D and 4E), as well as formation of abundant partially deformed quartz veins.

RETROGRESSIVE MICROFABRICS

More than 50 samples from different sections across Naxos were analyzed (Table 1; for locations, see Fig. 2). All thin sections of samples were cut parallel to the kinematic *x-z* section (that is, parallel to the stretching lineation and normal to the foliation). Here, we distinguish retrogressive microfabrics within (1) the relict high-pressure rocks in the southeastern and the interior parts of the Naxos metamorphic core complex, (2) the Melanes shear zone, and (3) the Naxos Granite.

Retrogressive Microfabrics within Relict High-Pressure Rocks of the Southeastern Region and in the Internal Naxos Metamorphic Core Complex

At least two deformation episodes are well preserved in the mica schists of SE Naxos. Early deformation is characterized by elongated garnet and feldspar grains and quartz grain aggregates, which imply deformation at relatively high-temperature conditions (Figs. 5A–5D). These rocks also underwent high-pressure metamorphism (e.g., detailed white mica chemistry can be found in Cao et al., 2013a). Retrogression, during a subsequent stage of shearing, is superimposed on the earlier high-temperature microstructures.

TABLE 1. MACRO- AND MICROSTRUCTURAL CHARACTERISTICS OF THE INVESTIGATED SAMPLES AND METHODS APPLIED TO INDIVIDUAL SAMPLES FROM THE NAXOS METAMORPHIC CORE COMPLEX

Location	Sample number	Latitude (°N)	Longitude (°E)	Rock type	Main microstructure of retrogression/overprinted deformation	Texture type		Microprobe	Ar-Ar dating
						Qtz	Cal		
East	N1A	37°05′00.7″	25°35′17.9″	Mylonitic quartzite	Qt: elongated and undulose extinction; Wm: grain-size reduction along discrete microshear zone; Cal: elongated coarse grains with grain-size reduction	Type III*	Type I	Chl*, Wm	Wm—fine grains
East	N1B			Mylonitic marble	Cal: grain-size reduction				
East	N1C			Mylonitic phyllite	Qtz: oriented/elongated with discrete zones of grain-size reduction; Wm: grain-size reduction along discrete microshear zone	Type II*		Chl*	
East	N1D			Mylonitic marble	Cal: fine grained		Type II*		
East	N2B	37°04′46.8″	25°35′20.9″	Mylonitic marble	Cal: fine grained				
East	N2E	37°04′46.8″	25°35′20.9″	Mylonitic marble	Cal: intense grain-size reduction		Type II		
East	N5			Mylonitic marble	Cal: coarse grains with irregular boundaries, thick twins overprinted by thin twins		Type I		
East	N6C	37°05′00.7″	25°34′35.5″	Mylonitic marble	Cal: grain-size reduction		Type I		
East	N11A	37°05′24.5″	25°35′30.0″	Mylonitic phyllitic mica schist	Qtz+Wm: S-C fabrics with intensive grain-size reduction; Pl: elongated and parallel porphyroclasts with fractures filled by Cal; Cal: elongated coarse grains with grain-size reduction	Type III*	Type I*	Chl	
East	N11B			mylonitic quartzitic phyllite	Qtz+Wm: grain-size reduction along discrete microshear zones			Chl*	
East	N11C			Calcite marble	Cal: grain-size reduction; Chl: sheared fine-grained aggregates with clear shear sense		Type II*	Chl	
East	N69A	37°04.858′	25°35.154′	Mylonitic mica schist	Qtz: grain-size reduction; Chl: sheared fine-grained aggregates within discrete microshear zones and clear shear sense				
East	N69B	37°04.858′	25°35.154′	Mylonitic marble	Cal: extremely fine grained		Type II		
East	N48	37°05.001′	25°34.712′	Banded marble	Cal: coarse grains with irregular boundaries and with bulging; grain-size reduction, thick and thin twins		Type I		
Southeast, high-pressure belt	N7A	36°59′43.0″	25°33′46.3″	Mylonitic marble	Cal: extremely fine grained, less twins		Type II*		
Southeast, high-pressure belt	N7B			Mylonitic marble	Cal: grain-size reduction with core-mantle structure, thin twins		Type I*		
Southeast, high-pressure belt	N7C			Mylonitic mica schist	Pl: elongated; Qtz: fine-grained aggregates; Wm+Chl: intensive grain-size reduction within discrete microshear zone; Cal: grain-size reduction	Type II	Type II*	Chl*	
Southeast, high-pressure belt	N9A	36°57′48.3″	25°33′01.7″	Mylonitic sericite quartzite	Qtz: slight elongation; Wm: grain-size reduction; Ser: along discrete microshear zone				
Southeast, high-pressure belt	N9B			Mylonitic marble	Cal: grain-size reduction and extremely fine-grained aggregates along discrete microshear zone		Type II*		
Southeast, high-pressure belt	N9C			Mylonitic marble quartz phyllite	Cal: fine-grained aggregates; Cal: coarse grains with grain-size reduction; Wm+Chl: intense grain-size reduction within discrete microshear zone; coarse Chl+Wm grains in microlithons	Type II*	Type I	Chl*	
Southeast, high-pressure belt	N10C	36°58′28.5″	25°35′26.1″	Mylonitic marble	Cal: intense grain-size reduction		Type II*		
South, high-pressure belt	N28	36°56′06.1″	25°28′30.3″	Mylonitic quartz-bearing mica schist	Qtz: elongated, undulose extinction and grain-size reduction; Wm: intensive grain-size reduction; fine-grained along discrete shear zones	Type III			
South, high-pressure belt	N29A	36°56′16.43″	25°28′26.9″	Mylonitic mica schist	Pl: elongated and oriented; Qtz: weakly elongated in aggregates; Wm: discrete shear zones with grain-size reduction; Cal: elongated coarse grains with grain-size reduction	Type II	Type I	Chl*	
South, high-pressure belt	N29B			Mylonitic banded marble	Cal: coarse elongated and oriented grains with grain-size reduction, cross twins				
Naxos core	N29C			Mylonitic quartzitic mica schist	Pl: elongated and oriented; Qtz: ribbons with undulose extinction and weakly elongated grains; Wm: discrete shear zones with grain-size reduction				
South, high-pressure belt	N30A	36°56′07.0″	25°20′29.8″	Mylonitic garnet-mica schist	Grt: weakly elongated and fracture filled with irregular mica, calcite, Qtz and Chl; Pl: elongated; Qtz: ribbon with intensive grain-size reduction; phengite and paragonite aggregates				
South, high-pressure belt	N30B			Mylonitic banded marble	Cal: coarse grains with irregular boundaries, thick and thin twins		Type I		

(*continued*)

TABLE 1. MACRO- AND MICROSTRUCTURAL CHARACTERISTICS OF THE INVESTIGATED SAMPLES AND METHODS APPLIED TO INDIVIDUAL SAMPLES FROM THE NAXOS METAMORPHIC CORE COMPLEX (*continued*)

Location	Sample number	Latitude (°N)	Longitude (°E)	Rock type	Main microstructure of retrogression/overprinted deformation	Texture type		Microprobe	Ar-Ar dating
						Qtz	Cal		
South, high-pressure belt	N31C	36°57′16.2″	25°28′26.8″	Mylonitic banded marble	Cal: coarse elongated and preferred oriented grains with grain-size reduction		Type I		
South, high-pressure belt	N32	36°57′52.7″	25°28′37.7″	Mylonitic sericite quartzite	Qtz: fine grains; Wm: fine-grained aggregates along discrete shear zone				
South, high-pressure belt	N33A	36°58′13.6″	25°28′53.4″	Mylonitic phyllonitic mica schist	Qtz: elongated or ribboned grained aggregates with grain-size reduction; Wm: fine-grained aggregates along discrete shear zone	Type II*			
South, high-pressure belt	N33B			Mylonitic quartzitic mica schist	Qtz: grain-size reduction, elongated coarse grains with bulging recrystallization; Wm: intensive grain-size reduction along discrete shear zone	Type II	Type I	Wm	Wm–fine grains
South, high-pressure belt	N58	36°56.105′	25°28.104′	Mylonitic mica schist	QTZ: weakly elongated grain ribbons or aggregates with grain-size reduction; Wm: sheared fine-grained aggregates along discrete shear zones	Type II			
South, high-pressure belt	N59	36°59.796′	25°31.169′	Mylonitic mica schist	Qtz: elongated grains with grain-size reduction; Wm: coarse grains sheared along discrete shear zone				
West, Melanes shear zone	N16A	37°05′50.1″	25°26′16.0″	Ultramylonitic mica schist	Qtz+Bt: extreme and homogeneous grain-size reduction				
West, Melanes shear zone	N16B			Ultramylonitic mica schist	Qtz+Bt: extreme and homogeneous grain-size reduction				
West, Melanes shear zone	N17A	37°05′43.4″	25°26′14.4″	Ultramylonitic amphibolite	Qtz+Bt: homogeneous grain-size reduction; Amp: elongated amphibole				
Western, Melanes shear zone	N17B			Mylonitic chlorite-bearing marble	Cal: dynamically recrystallized grains and elongated porphyroclasts with typical core-mantle structure; Chl: aggregates along discrete shear zone and veins			Chl	
Near migmatite dome	N24	37°28′31.0″	25°27′59.6″	Mylonitic aplite gneiss	Qtz: ribbons or aggregates; Pl: elongated coarse grains with bulging recrystallization; Wm: sheared coarse grains and dynamic recrystallization; discrete shear zones with grain-size reduction; Chl: sheared in fractured Pl and tails.	Type I*			Wm–fine grains
North	N52	37°10.096′	25°29.255′	Orthogneiss	Pl: elongated; Qtz: distributed grain-size reduction; Wm: sheared fine-grained aggregates along discrete shear zone	Type I			
North	N53B	37°11.356′	25°31.300′		Cal: elongated coarse grains with irregular boundaries and thin twins		Type I		
North	N54	37°11.635′	25°31.439′	Coarse-grained marble	Cal: coarse grains with irregular boundaries and locally bulging recrystallization, cross thick and thin twins		Type I		
Center	N56A	37°02.689′	25°30.371′	Medium-grained marble	Cal: coarse grains with irregular boundaries and grain-size reduction along discrete shear zone		Type I		
Center	N57A	37°00.949′	25°29.040′	Mylonitic quartzite	QTZ: weakly elongated grain aggregates; Wm: sheared fine-grained aggregates along discrete shear zone	Type I			
Center	N57B	37°00.949′	25°29.040′	Mylonitic recrystallized marble	Cal: coarse grain with irregular boundaries and bulging recrystallization, cross thick and thin twins		Type I		
Center	N60	37°00.940′	25°28.826′	Mylonitic quartzite	Qtz: weakly elongated ribbons or aggregates, locally bulging recrystallization along discrete shear zones; Wm: intensive fine grain along discrete shear zones	Type II			
Center–migmatite dome	N62	37°05.395′	25°28.002′	Coarse marble	Cal: large coarse grain with lots of thin twins, locally bulging recrystallization, cross thick and thin twins		Type I		
Center–migmatite dome	N63B	37°05.234′	25°29.733′	Coarse-grained marble	Cal: elongated coarse grain with irregular boundaries and grain-size reduction, thick and thin twins		Type I		
Center–dome	N64	37°05.478′	25°30.874′	Mylonitic orthogneiss	Qtz: ribbons, serrated high-angle and straight low-angle boundaries; distributed shear zones with grain-size reduction of Qtz and Bt	Type II			
Center	N65	37°08.716′	25°32.125′	Mylonitic Bt-gneiss	Qtz and Bt: zones of grain-size reduction; Pl: porphyroclasts	Type II			
Center	N66	37°09.673′	25°33.326′	Mylonitic Bt-gneiss	Qtz: ribbons, serrated high-angle and straight low-angle boundaries; distributed shear zones with grain-size reduction of Qtz and Bt	Type III			
Center	N67			Mylonitic marble	Cal: grain-size reduction		Type I		
West, granodiorite	N71	37°06.565′	25°23.042′	Chloritized granodiorite	Pl+Kfs: elongated coarse grains with myrmekite, S-C fabrics; Chl: sheared			Chl	
West, granodiorite	N72A	37°05.395′	25°24.354′	Granodiorite	Pl+Kfs: elongated coarse grains with myrmekite; Hb: strong elongated and sheared; rare distributed microshear zones with grain-size reduction			Amp+Pl	

Note: Pl—plagioclase, Kfs—K-feldspar, Qtz—quartz, Wm—white mica, Bt—biotite, Chl—chlorite, Cal—calcite, Grt—garnet, Ser—sericite, Amp—amphibole.
*Data from Cao et al. (2013a).

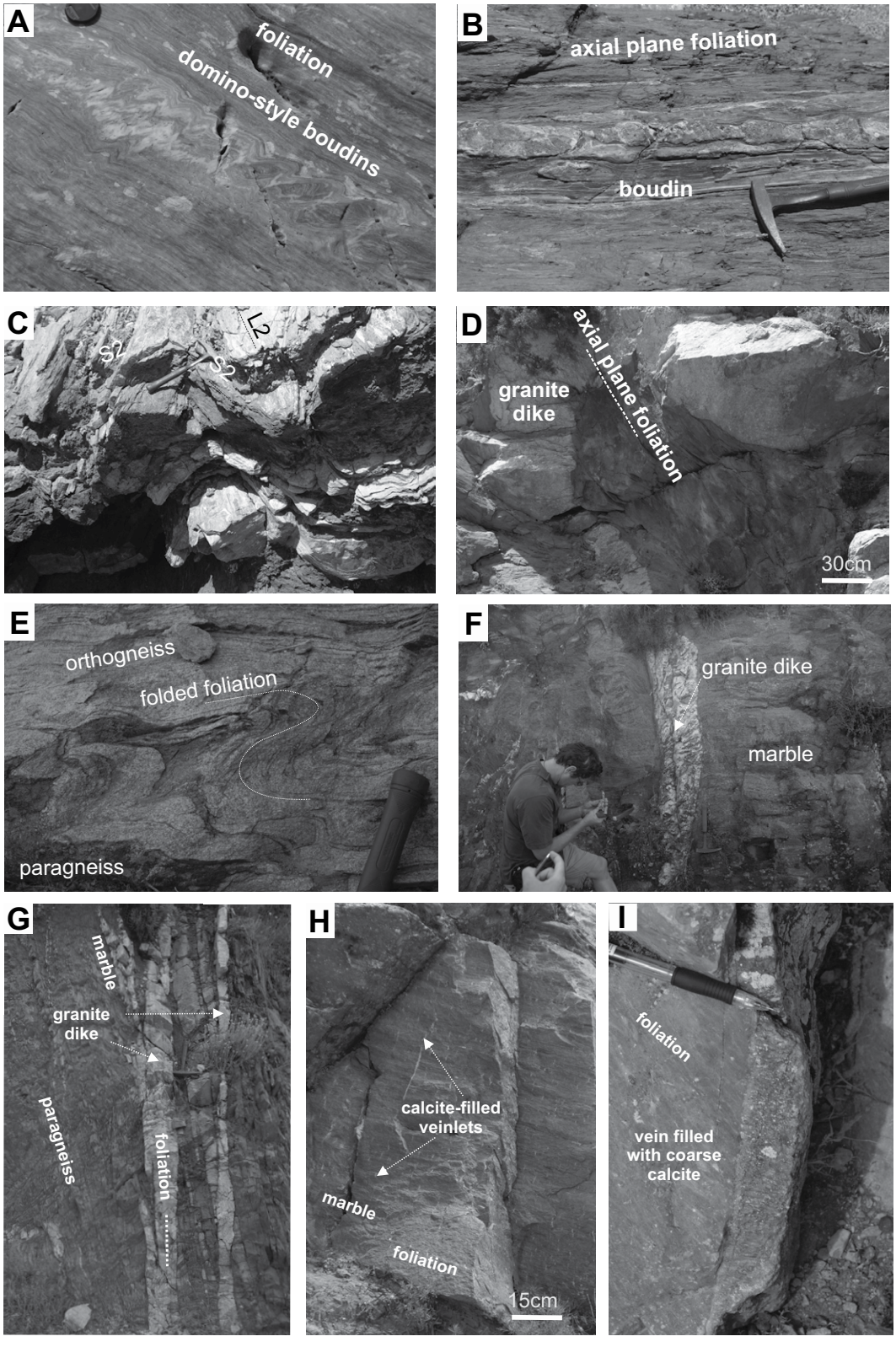

Figure 3. Field photographs of structures formed during retrogression in the interior of the Naxos metamorphic core complex. (A) Domino-style boudinage within marble. (B) Foliated calc-schist with a foliated calcite marble layer with dolomite marble lenses. (C) Open folds within schists. (D) Folded granitic dike within schist and axial plane foliation crosscutting the schist and granitic dike. (E) Large-scale fold hinges with gently E-dipping axial surfaces on the ridge east of Mount Zas. (F) Subvertical, internally deformed and foliated late-stage granite dike cutting the main foliation S_1 of a marble. (G–I) Dikes and veins within the Naxos metamorphic core complex. (G) Subvertical granite dike within the succession of paragneiss and marble. Some of dikes bear a weak N-S–trending subvertical internal foliation. (H) Subvertical calcite-filled veinlets oriented perpendicular to the main foliation within marble. (I) Subvertical late-stage E-W–striking extensional vein filled with coarse isometric epitaxial (rim) and elongated calcite crystals (east of Mount Zas).

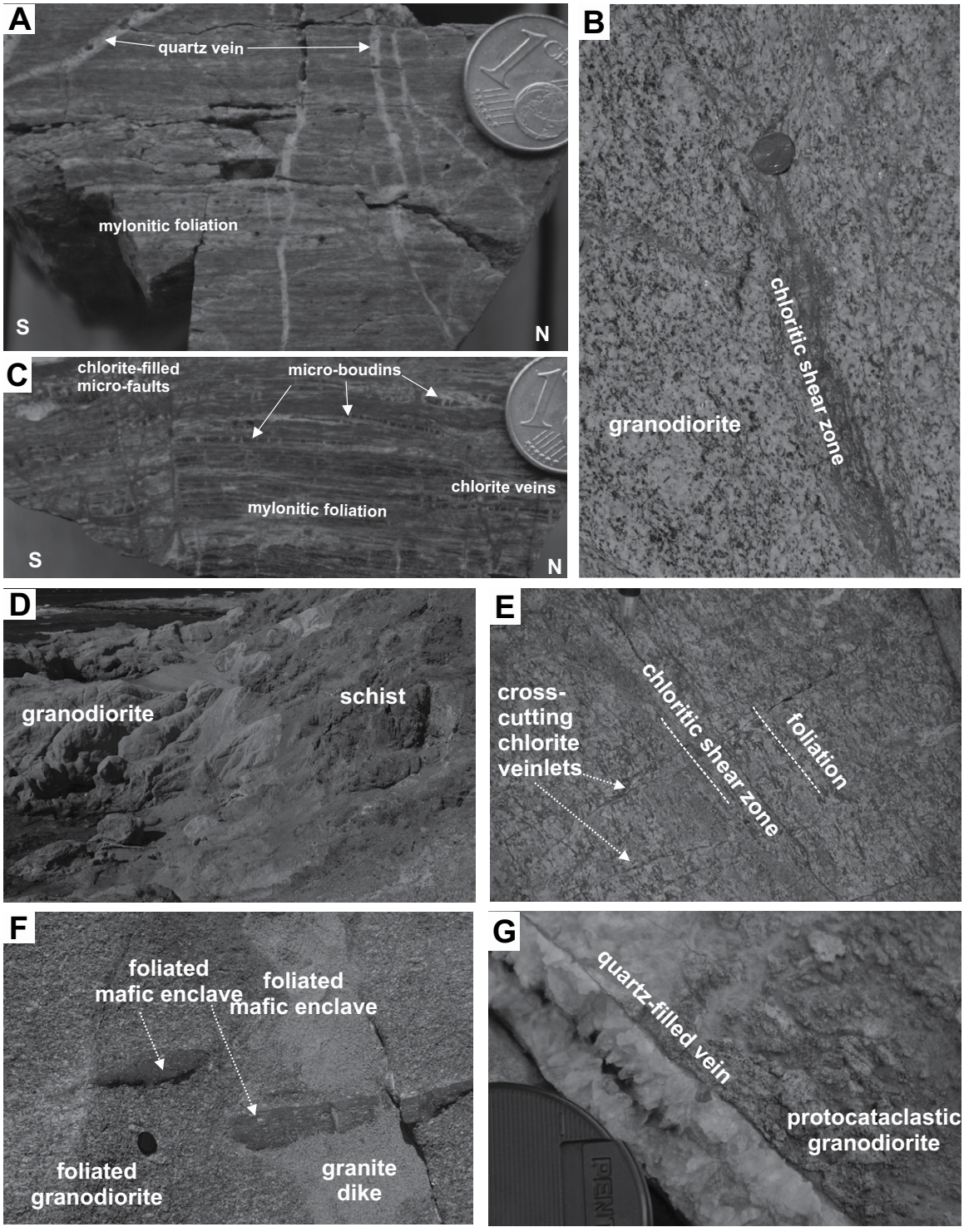

Figure 4. Field photographs of structures within Melanes shear zone (A–B) and the Naxos Granite (C–G). (A) Mylonitic paragneiss with numerous quartz veins crosscutting the foliation. (B) Mylonitic paragneiss with microboudins, chlorite veins, and subvertical microfaults filled by chlorite. (C) Intrusive contact between the Naxos Granite and schists of the Naxos metamorphic core complex in southwestern Naxos. (D) Chloritic shear zone within partly retrogressed Naxos Granite to the east of the town of Naxos. (E) Foliated granodiorite and chloritic shear zone within partly retrogressed Naxos Granite, showing brittle faults crosscutting chlorite veinlets. (F) Granite dike within foliated Naxos Granite. The foliated granitic dike postdates foliation within granodiorite and mafic enclaves, suggesting high ductility of mafic enclave during granite dike emplacement. (G) Protocataclastic granodiorite and extensional vein filled with epitaxial euhedral quartz growing into an open gash.

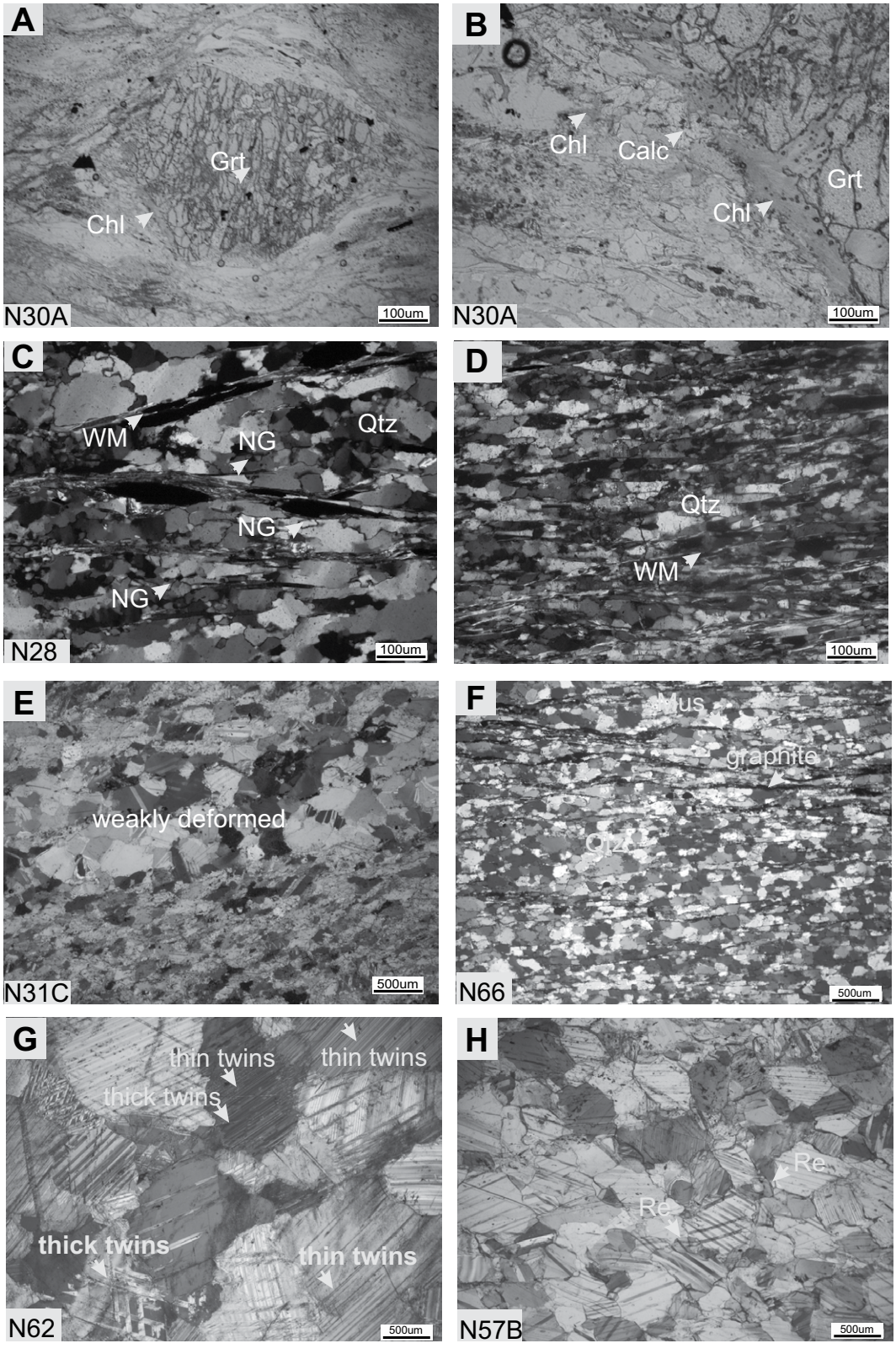

Figure 5. Retrogressive microfabrics formed by overprinting high-temperature deformation in relict high-pressure metamorphic zone in southern Naxos Island (A–E) and in the interior of the Naxos (F–H). (A) Two stages of metamorphism preserved in the garnet–mica schist. Elongated garnet (Grt) surrounded by sheared white mica aggregates. Retrogression is especially characterized by fractured garnet and infill by chlorite (Chl) in strain shadows of garnet during shearing. (B) Chlorite (Chl) flakes fill the fracture of the garnet (Grt) and wrap around the boundary of the garnet. (C) Small dynamically recrystallized grains, subgrains, and elongated quartz (Qtz) aggregates with relatively irregular boundaries in the mica schist. Small subgrains (NG) are developed along the boundary of quartz mainly by bulge recrystallization at low-temperature conditions. Image also shows a new discontinuous foliation formed by recrystallized white mica (WM) aggregates and opaque minerals. (D) New discontinuous, anastomosing foliation formed by fine-grained white mica aggregates and opaque minerals. (E) Irregular or serrated grain boundaries of calcite with elongation oriented parallel to the shear plane. Weakly deformed calcite grains are locally preserved. (F) A new discontinuous foliation formed by the recrystallized white mica aggregates, graphite, and opaque minerals. Bulged recrystallized fine grains occur at the boundary of coarse quartz grain. (G) Thin twins overprinting coarse-grained calcites. Coarse calcite grains show serrated grain boundaries. (H) Coarse-grained calcite grains with bulged recrystallized fine grains along boundaries.

Stretched early garnet grains with intragranular fractures are filled with irregular biotite, calcite, quartz, and chlorite (Figs. 5A and 5B). The quartz microstructures were affected by low-temperature deformation, as evidenced by fine recrystallized grains formed by bulge recrystallization and rare occurrences of small grains (new grains or subgrains) at the triple junctions of the larger quartz grains (Figs. 5C and 5D). A second generation of recrystallized white mica includes fine grains generally concentrated in microscale shear zones (Figs. 5C and 5D). Calcite grains in marble are characterized by coarse grains (Fig. 5E) formed by high-temperature growth that are often dominated by thin twins. However, the coarse grains show serrated and irregular boundaries and recrystallized small grains around the elongated relict grains.

Microstructures show early high-temperature plastic deformation of the main mineral phases, which still are locally preserved in these mylonitic rocks (Fig. 5F) and in coarse-grained marbles (e.g., Figs. 5G and 5H) located near migmatites. Quartz grains, often in ribbon and elongated grain aggregates, are the most common high-temperature microstructures in the sheared schists. Ribbon or coarse-grained quartz is replaced by bulged recrystallized fine grains during retrogression. Some relict early coarse biotite grains surrounded by fine grains of quartz and biotite show sigma fabrics indicating a top-to-the-N shear sense. Early host white mica grains have been progressively deformed by recrystallization to an aggregate of fine-grained mica neoblasts oriented parallel to the mylonitic foliation and lineation in shear zones (Fig. 5F). Coarse calcite grains formed during high-temperature deformation exhibit serrated and irregular boundaries, with recrystallized grains showing straight to diffuse and irregular grain boundaries (Figs. 5G and 5H). These larger grains bear several sets of twins or show polyphase twinning (twins in twins) at different angles, possibly indicating that they were caused by multiple deformation stages. Type III and IV twins (according to Ferrill et al., 2004) only occur in large grains. Most calcite twins are thin and straight, similar to types I and II of Ferrill et al. (2004), and are related to low-temperature deformation. Shear bands, sigma-type mica porphyroclasts, and mica fish consistently indicate bulk top-to-the-N shearing related to low-temperature retrogressive deformation.

Retrogressive Microstructures within the Melanes Shear Zone

Mylonitic amphibolite of the Melanes shear zone (Fig. 4) shows relict lens- or fish-shaped amphibole porphyroclasts, homogeneously fine-grained amphibole, biotite, and quartz aggregates, constituting the foliation and stretching lineation (Figs. 6A and 6B). Undulatory or inhomogeneous extinction occurs in relict porphyroclasts. A few relict elongated feldspar grains show cataclastic fabrics (Fig. 6A). Dramatic grain-size reduction of the main minerals (0.1 mm) is observed microscopically within mylonitic amphibolite and even in mica schist (Figs. 6A–6B) and is interpreted to be the result of a late-stage regional low-temperature retrogressive event. The microstructure of mylonitic marble is dominated by elongated, undulose, twinned, and kinked calcite porphyroclasts surrounded by dynamically recrystallized grains producing a typical core-mantle structure. Thin twins are widespread, and undulose extinction is conspicuously absent in these calcite grains. In marbles, further retrogressive microfabrics are present in the extensional veins filled by chlorite, quartz, and/or calcite (Figs. 6C and 6D). Most sheared chlorite aggregates form a new continuous or discontinuous foliation (Fig. 6D).

Retrogressive Microstructures within the Naxos Granite

The granodiorites at margins of the Naxos Granite body experienced shear deformation to form protomylonitic rocks (Fig. 6E) containing K-feldspar, plagioclase, amphibole, quartz, and chlorite. Incipient S-C fabrics are present in the mylonitic granodiorite, with the S plane defined by grain aggregates of K-feldspar and plagioclase, amphibole, quartz, biotite, and chlorite, and the C plane defined by strongly elongated K-feldspar and plagioclase grains (Fig. 6E). The acute angle between S and C is generally 10°–25°. The protomylonitic S-C fabric relates to late solid-state low-temperature deformation conditions. The alignment of feldspar crystals suggests that the fabric partly represents a magmatic foliation, but recrystallization of quartz indicates that solid-state deformation has been superimposed on the magmatic grains. Microcracks infilled by new-formed chlorite (Fig. 6E) in some feldspar porphyroclasts formed semibrittle to brittle microstructures during retrogression.

CRYSTALLOGRAPHIC PREFERRED ORIENTATIONS (CPOs) RELATED TO RETROGRESSIVE FABRICS

Quartz CPOs

Quartz fabrics are generally demonstrated by *c*-axis crystallographic preferred orientation (CPO) patterns or *c*-axis pole figures (Fig. 7). Quartz CPOs analysis was conducted on 18 mylonitic quartz-rich rocks from the Naxos metamorphic core complex (Table 1), of which six samples are from an earlier paper (Cao et al., 2013a). Four basic types of quartz *c*-axis fabrics are recognized, which reflect different quartz microstructures: type I, close to *y* maxima; type IIa, crossed girdles with maxima close to the *y* axis; type IIb, crossed girdles with maxima between the *x* and *z* axes; and type III, single girdles (Schmid and Casey, 1986).

Fabrics of type I are characterized by one or two maxima close to the *y* axis (Fig. 7, e.g., N52, N57, N24), which resulted from prism <*a*> slip, a medium-temperature deformation mechanism (Stipp et al., 2002). However, some maxima are elongated, which is likely the result of a combination of rhomb <*a*> slip and low-temperature basal <*a*> slip (Schmid and Casey, 1986; Stipp et al., 2002). The low-temperature overprint on minerals in these samples is also indicated by the microstructure, including bulging recrystallization of quartz, extreme grain-size reduction, and formation of white mica fish and of a second generation of fine-grained white mica. Krabbendam et al. (2002) claimed that some fine-grained quartz-rich shear zones were actually high grade, and the grain size was pinned by secondary phases (graphite). The maxima are primarily distributed asymmetrically around the *y* axis, which may be related to a late stage of noncoaxial shear, although the relationship between the quartz crystallographic fabric geometry and finite strain geometry is not straightforward (Sullivan and Beane, 2010). Type II fabrics are characterized by complex asymmetrical superposition fabrics with one or two maxima close to the *y* axis and asymmetrical girdle axis (type IIa: N64, N65, N33, N29A, N1C) and crossed girdles with maxima between *x* and *z* (type IIb: N60, N58D, N33B, N7C, N32, N9C). Type IIa fabrics present the maximum in the center (*y*) and the weaker submaxima distributed on a great circle (*x*-*z*), between the maxima, with a large opening angle of 65° and a smaller opening angle between 20° and 45°, indicative of high- to middle-temperature deformation with dominant combined prism <*c*> and rhomb <*a*> slip (e.g., Schmid and Casey, 1986). The weak submaxima in the fabrics considered here were attributed to a basal <*a*> slip low-temperature superimposition during subsequent deformation (Stipp et al., 2002), consistent with microscopic observations. Type IIb fabrics shows a weak maximum close to *y*, and one or two maxima are distributed in the *x*-*z* plane. The patterns indicate activity of basal <*a*> slip and weak rhomb <*a* + *c*> slip systems, with less frequent prism <*a*> slip, suggesting a strong low-temperature deformation overprint during medium-temperature deformation. These asymmetric girdle fabrics passing through the *y*-direction are observed in the mylonitic rocks,

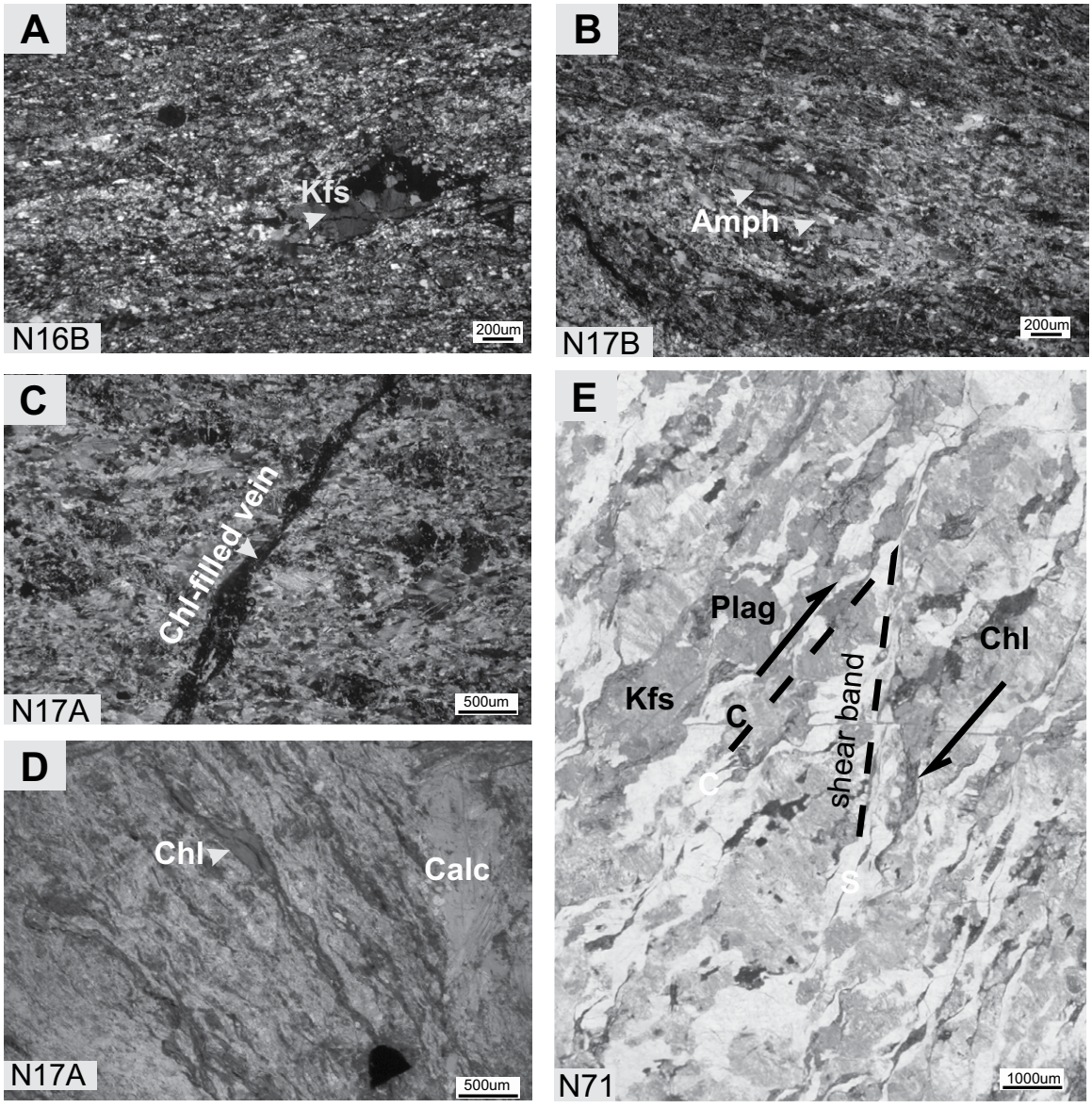

Figure 6. Retrogressive microstructure within the Melanes shear zone (A–E) and within the Naxos Granite (F–G). (A–B) Extremely fine-grained amphibole (Amph), mica, and quartz grains, K-feldspar (Kfs), and a few relict elongated amphibole grains in the ultramylonitic amphibolite and mica schist. (C) Chlorite (Chl)–filled vein crosscutting the foliated marble. (D) Coarse- and fine-grained chlorite in the mylonitic marble. (E) S-C fabric in the mylonitic granodiorite, where S plane is defined by grain aggregates of two feldspars (K-feldspar [Kfs] and plagioclase [Plag]), quartz, and chlorite, and C plane is defined by strongly elongated grains of two feldspars. (G) Sheared chlorite indicating shear sense.

which are ascribed to coaxial strain (Passchier and Trouw, 2005). Type III fabrics are characterized by asymmetric single girdle fabrics passing through the *y*-direction, and the concentrations of *c*-axes are close to the *z* axis (N66, N28, N11A, N1A). The single girdle patterns show clockwise rotation with respect to the *x*-*z* plane, suggesting dominant activation of <*a*> basal slip at lower temperatures, possibly within lower-greenschist-facies conditions. The slightly asymmetric patterns record a significant component of noncoaxial top-to-the-NNE sense of shear deformation (Fig. 7), consistent with information presented by Krabbendam et al. (2002).

Calcite CPOs

Calcite CPOs analysis was conducted on 24 mylonitic marbles from the Naxos metamorphic core complex. All calcite *c*-axis textures and sample locations are presented in Figures 8 and 9.

Calcite microstructures of these samples from the interior of the Naxos metamorphic core complex show protomylonitic fabrics with coarse calcite porphyroclasts surrounded by later recrystallized smaller grains. In most samples, coarse grains show serrated and irregular boundaries and are elongated slightly oblique to the foliation. The CPO is characterized by

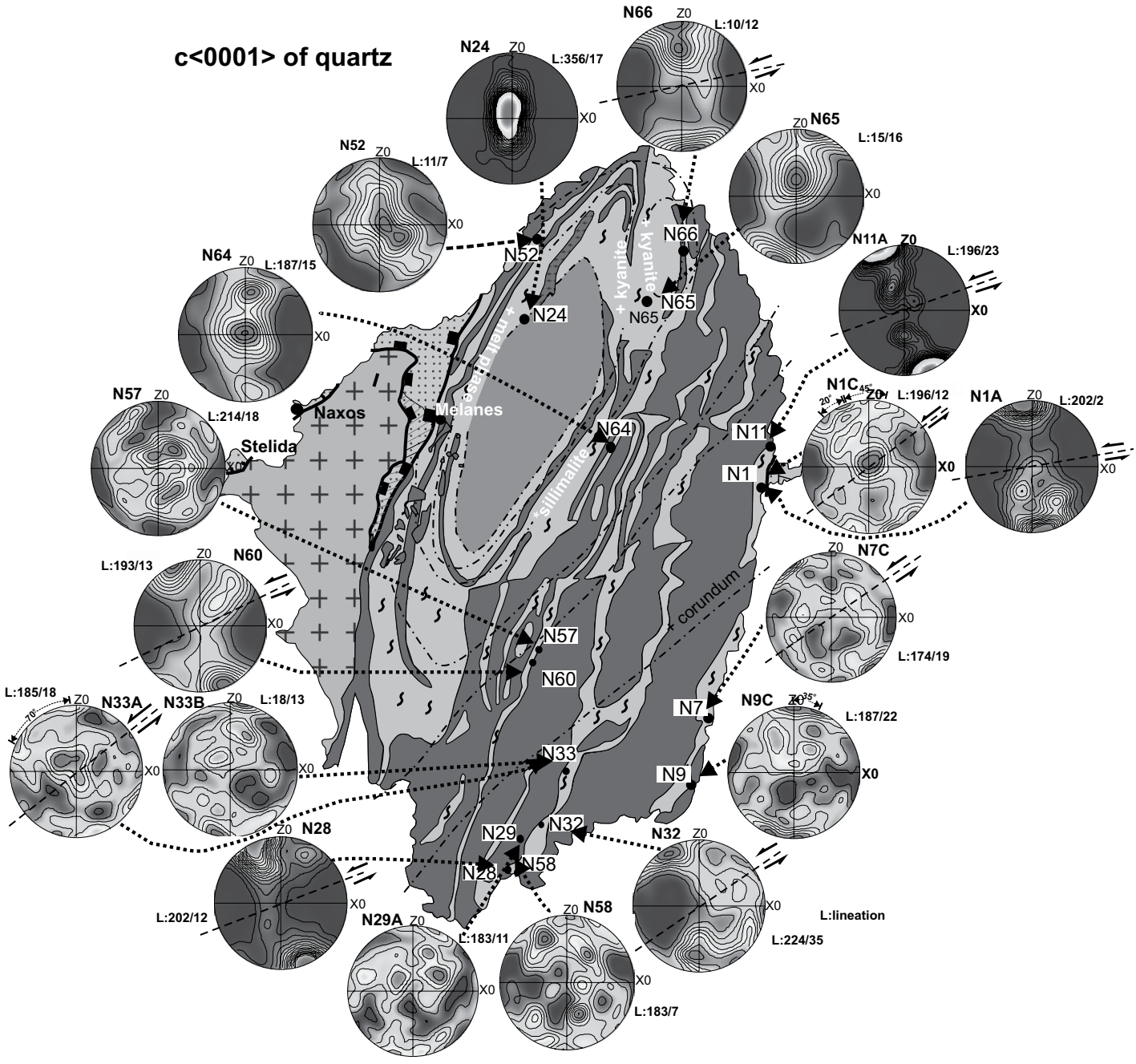

Figure 7. Quartz-*c* axis textures from partially retrogressed rocks (measured by backscattered electron diffraction). Equal-area, lower-hemisphere projections are contoured at uniform interval distributions. Foliation is horizontal, and lineation is in plane in the E-W direction. The locations of samples are shown in Figure 2. Samples N1C, N1A, N11A, and N9C are from eastern Moutsounas shear zone, N24 is from near a migmatite dome, and N33A is from a high-pressure belt for comparison (taken from Cao et al., 2013a).

a broad *c*-axis <0001> maximum close to the *z* plane and a weak girdle in *y*-*z*, which is subnormal to the foliation plane. The <*a*> axis is distributed within a girdle in the *x*-*y* shear plane, and the *e* planes are relatively weakly distributed on a similarly oriented axis. This supports the fact that the calcite texture presented in this paper developed by intracrystalline slip (dominated by *c* slip) and *e*-twinning under low-temperature conditions (Cao et al., 2013a). In calcite, the *c*-axis maximum rotated against the shear sense with respect to the main shear plane observed in porphyroclasts and recrystallized grains. The asymmetry indicates top-to-the-N–directed shear. Most samples from the eastern boundary are ultramylonites with a fully recrystallized microstructure. The small calcite grains from most samples show strong CPOs with a single *c*-axis maximum subperpendicular to the foliation. The *a* planes form a girdle subparallel to the foliation, and *e* planes exhibit a weak single maximum similar to the *c* axis and are orientated nearly perpendicular to the foliation plane.

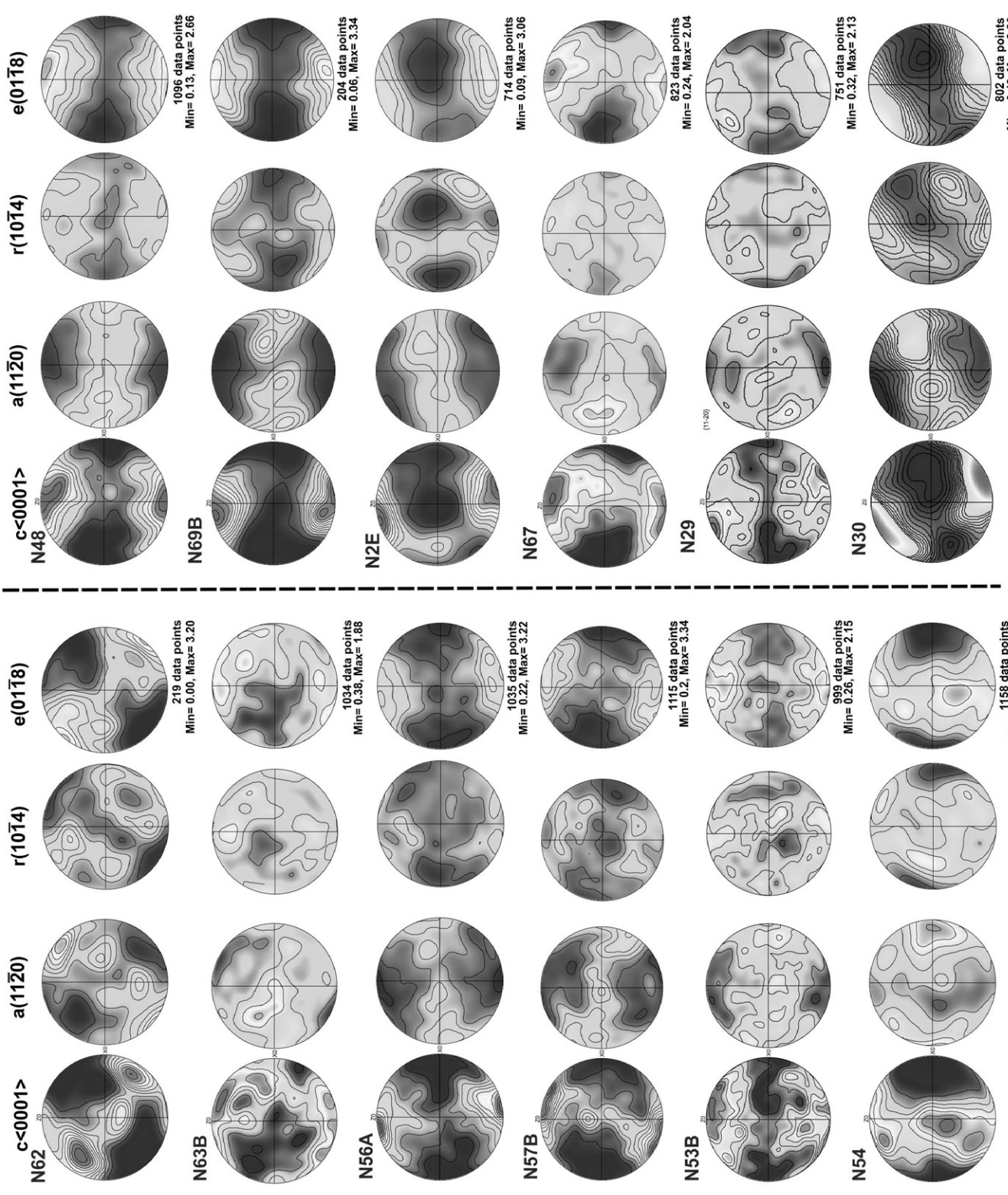

Figure 8. Calcite textures from retrogressed rocks measured with backscattered electron diffraction. Equal-area, lower-hemisphere projections *are* contoured at uniform interval distributions. Foliation is horizontal. and lineation is in plane in the E-W direction. The number of calcite analyses (*n*) in each sample is shown.

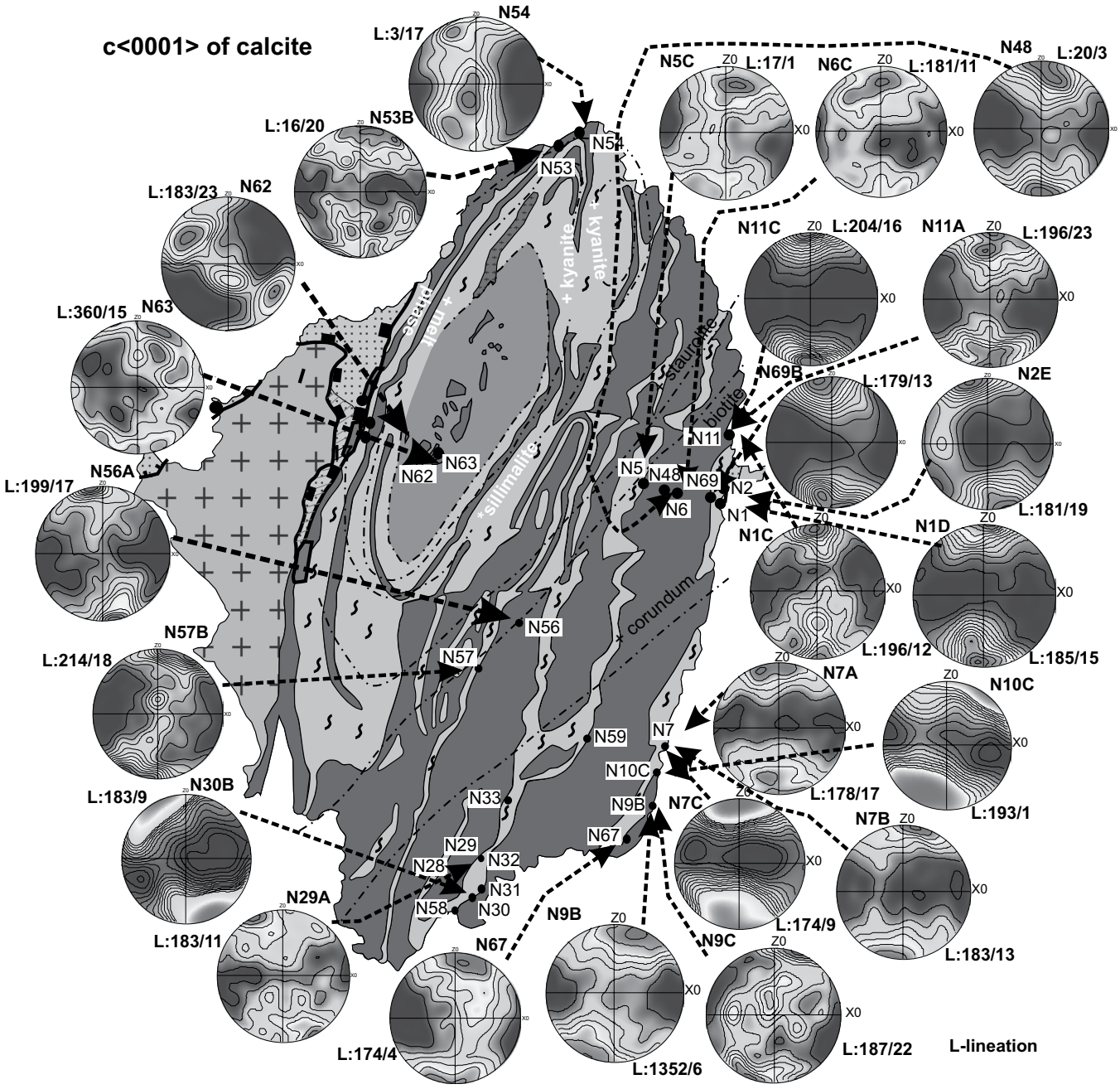

Figure 9. Calcite *c*-axis textures from partially retrogressed rocks measured with backscattered electron diffraction. Equal-area, lower-hemisphere projections are contoured at uniform interval distributions. Foliation is horizontal, and lineation is in plane in the E-W direction. The locations of samples are shown in Figure 2. Samples N1D, N7A, N11C, N7C, N9B, N5C, N6C, N7B, N1C, N11A, N9C, and N10C, mainly from eastern Moutsounas shear zone, are, for comparison, taken from an earlier paper (Cao et al., 2013a).

CONDITIONS OF METAMORPHISM DURING RETROGRESSION

Hornblende-Plagioclase Thermometry of Granodiorite (Naxos Granite)

The Al content in hornblende (aluminum-in-hornblende barometry) is commonly used with coexisting hornblende and plagioclase (hornblende-plagioclase thermometry) in a paragenesis also containing quartz and K-feldspar to constrain the pressure and temperature during the crystallization of an intermediate magma or subsequent metamorphism. Chemical compositions of plagioclase and hornblende of sample N72 from a granodiorite of the Naxos Granite are given in Table DR1.[1] Based on hornblende solid-solution models and well-constrained natural and experimental systems, the temperature was calculated by application of the hornblende-plagioclase geothermometer of

[1]GSA Data Repository item 2016294, Tables DR1–DR5, is available at http://www.geosociety.org/pubs/ft2016.htm or by request to editing@geosociety.org.

Holland and Blundy (1994) and the pressure by the Al-in-hornblende geobarometer of Schmidt (1992), Anderson (1996), and Ridolfi and Renzulli (2012). The calculated temperature is in the range from 661 °C to 583 °C, and the average is 621 ± 19 °C. The calculated pressures mainly range from 1.70 to 1.24 kbar, and the average is 1.5 ± 0.2 kbar, representing the lithostatic pressure during emplacement of the granodiorites of the Naxos Granite (Gautier et al., 1993).

Two-Feldspar Thermometry

A few samples from the Naxos metamorphic core complex and foliated Naxos Granite contain both sodic and potassic feldspar. The thermometry for samples N71, N53, and N61 was done using microprobe analyses of two coexisting feldspars according to the method of Perchuk et al. (1991). In the case of the Naxos Granite, we used the pressure during intrusion of ~1.5 kbar to calculate the disequilibration of temperature (Table DR2 [see footnote 1]). For sample N71, with coarse-grained colorless plagioclase and flesh-colored K-feldspar, we calculated a temperature range from 539 °C to 238 °C, which implies reequilibration under variable temperatures after solidification (Table DR2 [see footnote 1]). Samples N61 and N53 are orthogneisses from the core of the Naxos metamorphic core complex, for which the calculated equilibration temperature ranges from 438 °C to 258 °C (N61), and from 334 °C to 214 °C (N53), suggesting low-temperature mineral equilibration.

Chlorite Thermometry–Related Microfabric Types

High-resolution backscatter electron (BSE) analyses allow better definition of the details of microfabrics in various types of chlorite-rich sheared rocks, discussed earlier (Table 1). Two deformed microfabric types were observed for the occurrences of chlorite and white mica from the samples (Fig. 10), (1) type I sheared, coarse-grained chlorite and white mica (D_1); and (2) type II sheared, fine-grained chlorite and white mica in the microshear zones (D_2).

The temperature of the shear zone parageneses can be estimated from the location of the following equilibrium (e.g., Cathelineau and Nieva, 1985): (clinochlore + sudoite)chl =

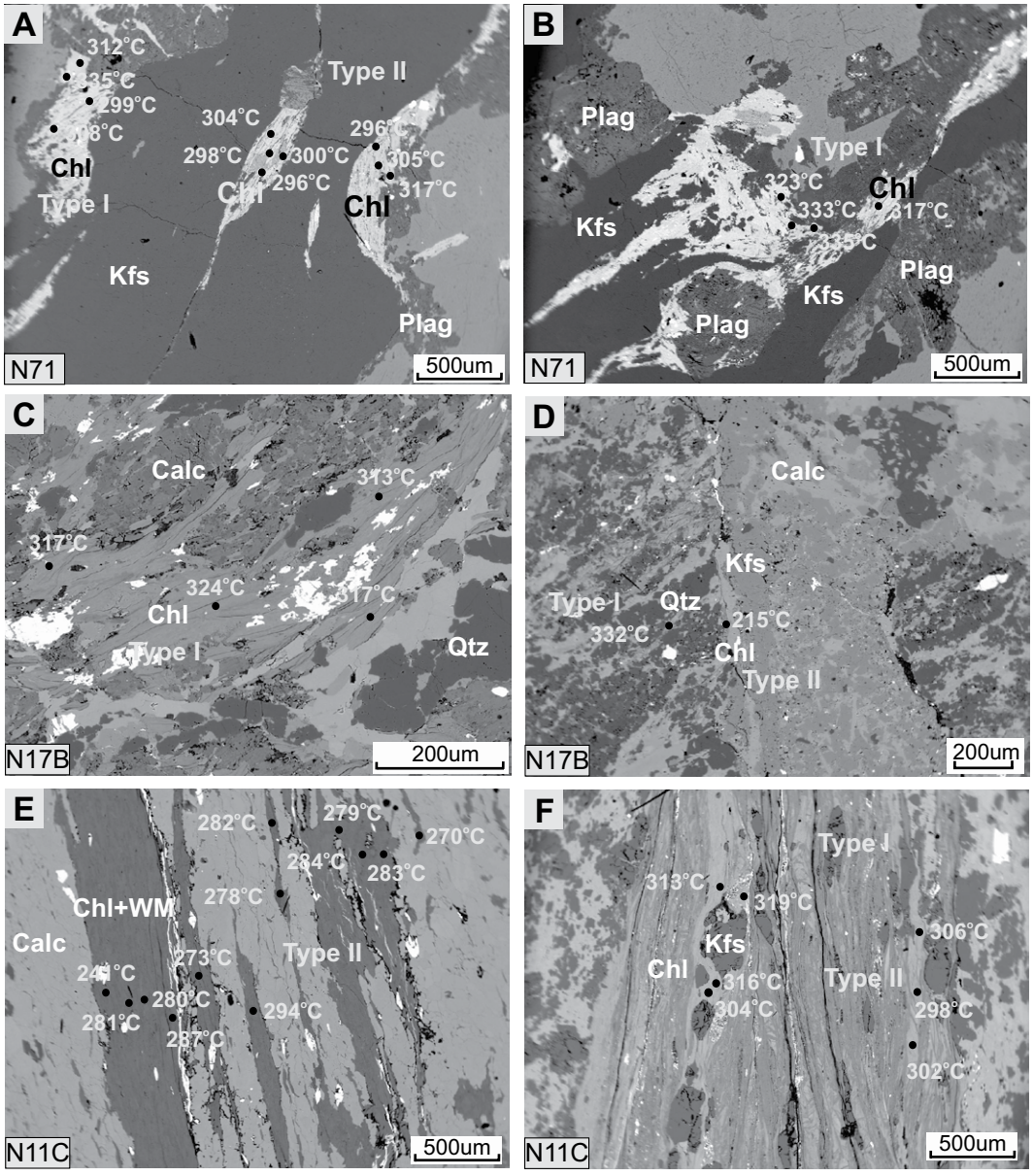

Figure 10. Backscattered electron microscopy images of microfabrics containing chlorite: (A–B) Images showing the two types of chlorite in sheared Naxos Granite; see text for explanation. (C–D) Images showing the two types of chlorite in sheared marbles within Melanes shear zone. (E–F) Images showing the two types of chlorite in sheared mica schists within eastern sectors of Naxos Island. Chl—chlorite; Kfs—K-feldspar; Plag—plagioclase; Calc—Calcite; WM—white mica; Qtz—Quartz.

(Mg-amesite)chl + quartz + H_2O. Temperature calculations were done using the chlorite solid-solution model and thermodynamic data from Vidal et al. (2001) and Vidal et al. (2005) assuming activity of water equal to unity. Conventional chlorite thermometry based on the Fe-Mg ratio of chlorite (Cathelineau and Nieva, 1985) was also done for comparison. Four chlorite-bearing samples from the middle (N17B), the eastern part (N11C), the northern region (N24), and one sample (N71) from the Naxos Granite were selected for chlorite thermometry analysis (Table DR3 [see footnote 1]; Fig. 10). Three different chlorite geothermometers were applied in this work: the geothermometer of Cathelineau (1988) (T1), based on the number of tetrahedral Al, and the geothermometers of Kranidiotis and MacLean (1987) (T2) and Jowett (1991) (T3), based on the number of tetrahedral Al and the Fe/(Fe + Mg) value. The Cathelineau (1988) (T1) equation yields results very similar to the methods presented in Kranidiotis and MacLean (1987) and Jowett (1991) (Table DR3 [see footnote 1]; results of geothermometers T1, T2, and T3; for more details, see Cao et al., 2013a, 2013b). Chlorite shows Si contents in the range of 3–2.5 a.p.f.u. (atoms per formula unit).

In most cases, the calculated temperatures yielded the following ranges: ~312–348 °C (D_1, T1) and ~274–303 °C (D_2, T1) for granodiorite sample (N71) from the western part, ~306–332 °C (D_1, T1) and ~215–298 °C (D_2, T1) for a marble sample (N17B) from the central part of the Naxos metamorphic core complex, ~293–321 °C (D_2, T1) and ~240–294 °C (D_2, T1) for chlorite-bearing marble samples (N11A, N11C) from the eastern part, and ~330–350 °C (D_1, T1) for mica schist from the northern part (N21). The chlorite temperatures from sample N24 range from 132 °C to 140 °C (D_3, T1). In the microfabric type II (D_2), the thermometry results from the sheared fine-grained chlorite grains yielded a temperature ranging from 321 °C to 215 °C, suggesting sub-greenschist-facies metamorphic conditions well below the temperatures usually considered to represent the brittle-ductile transition zone (~300 °C).

White Mica Compositions and Barometry

According to microstructures based on BSE analysis (Fig. 11), intensely recrystallized fine-grained white micas were observed along discrete microshear zones in our dated samples (see next section). The compositional results of representative analysis of white mica from the $^{39}Ar/^{40}Ar$ dated samples (N33B, N1A, N1C, N24) are given in Table DR4 (see footnote 1). The analysis of white mica from the four samples indicates the compositions of various types of white mica reflect diverse origins and times of growth. White micas in sample N33B have a dominance of low Si at ~6.08–6.17 a.p.f.u. and, therefore, muscovite composition. One grain presented a high Si value at ~6.69 a.p.f.u. with phengitic composition. White micas from samples N1A and N1B yielded a wide range of compositions of Si from ~6.23 to 6.40 a.p.f.u. and have, therefore, muscovite composition with a low Si a.p.f.u. and phengite composition with a low Si a.p.f.u., respectively Coarse-grained white micas in sample N1C yielded a dominance of high Si at ~6.55–6.97 a.p.f.u. and have, therefore, phengite composition. Some phengitic compositions with high-Si white micas also occur in the sheared zones. Fine-grained white micas in sample N24B yielded a dominance of low Si at ~6.14–6.18 a.p.f.u. and, therefore, muscovite composition. We note that phengite is, therefore, inherited from high-pressure metamorphism, and it was only rarely reset to low-pressure muscovite during shearing and exhumation. The muscovite grains with a low Si value at ~6.2 a.p.f.u. (Table DR4 [see footnote 1]) yielded mainly low-pressure conditions (<2.5 kbar).

WHITE MICA $^{40}Ar/^{39}Ar$ DATING

White mica concentrates were prepared from four samples from the southern relict high-pressure rocks (sample N33B), the eastern boundary (samples N1A and N1C), and the northern part (sample N24). The $^{40}Ar/^{39}Ar$ analytical technique is described in Appendix A3, and the analytical results are given in Table DR5 (see footnote 1) and Figure 12. The compositions of white micas in dated samples were also analyzed with electron microprobe (see previous sections).

Sample N33B from the southern relict high-pressure belt, south of the corundum-in isograd of M2 metamorphism, is a deformed fine-grained mica schist (Figs. 12A and 12B). Small, newly formed white mica grains (<250 μm) that crystallized during retrogressive deformation were sampled to investigate the extent of resetting of the Ar isotopic system in the preexisting white mica. The Ar release pattern resulted in a plateau age of 16.52 ± 0.39 Ma (steps 5–10 including 87% of ^{39}Ar released; Fig. 12A). Isotope inversion resulted in an age of 16.3 ± 1.2 Ma (with a $^{40}Ar/^{36}Ar$ initial value of 324 ± 120 Ma; Fig. 12B). We therefore consider the plateau age of 16.52 ± 0.39 Ma to be geologically significant and to date the formation age during retrogression within greenschist-facies conditions after peak M2 metamorphic conditions.

Sample N1A is a mylonitic quartzite close to the upper boundary of the Moutsounas shear zone along the eastern boundary of the Naxos metamorphic core complex. In this sample, mica grains are fully recrystallized and mostly fine grained (<100 μm), and almost no porphyroclasts are present (Figs. 12C and 12D). Polycrystalline and elongated quartz aggregates are common due to recrystallization. The recrystallized quartz and white mica aggregates with opaque minerals form a continuous or discontinuous foliation and stretching lineation. The argon release pattern of the white mica concentrate of rare larger grains results in a pattern with two age groups. A plateau age of 14.34 ± 0.36 Ma (steps 2–6 including 65.1% of ^{39}Ar released; Fig. 12C) can be juxtaposed with another mean age of 20.1 ± 1.4 Ma (steps 7–11 including 30% of ^{39}Ar released). Isotope inversion of all steps resulted in an age of 12.6 ± 0.28 Ma (with a $^{40}Ar/^{36}Ar$ initial value of 713 ± 240 Ma; Fig. 12D), showing significant excess argon. We think that the sample consists of micas of two different age populations, although we cannot exclude the presence of excess Ar in the older population. We consider that the to plateau age of 14.34 ± 0.36 Ma of the low-temperature steps approximately dates Ar loss of older grains during shearing.

In the thin section of sample N1C, we observed that the mica grains are substantially more affected by recrystallization than micas from adjacent rocks (e.g., sample N1A). The age spectrum of sample N1C shows a staircase pattern ranging from an age of ca. 5 Ma to a maximum of 50 Ma, all with high analytical uncertainties because of the low gas yield due to the small grain size (Fig. 12E). We interpret this pattern as mixture between two or three age components, including a possibly untrustworthy young age component at 5–14 Ma (with a too low radiogenic component of <12% $^{40}Ar^*$), one at ca. 50 Ma, and a third that could be deduced from a mean age of 30.7 ± 3.5 Ma from the last four steps. To assess potential age components, we performed single-grain total fusion experiments on several further single grains (with only one or five steps because of the low gas yield due to the small grain size and young age). The experiments N1C-exp1 and N1C-exp2 (Figs. 12F and 12G) show staircase patterns, and ages as low as ca. 13.9 ± 0.9 Ma and 11.9 ± 0.8 Ma in the initial steps of the experiments and well-constrained ages of 24.5 ± 2.0 Ma and 19.3 ± 1.0 Ma. Finally, a total fusion experiment (experiment 3) on a small single grain yielded an age of 38.3 ± 4.2 Ma. The staircase patterns clearly show Ar loss of older mica grains, which possibly formed during M2 or M1 (experiment 3) metamorphism (Figs. 12E and 12F) during final shearing at elevated temperatures. This

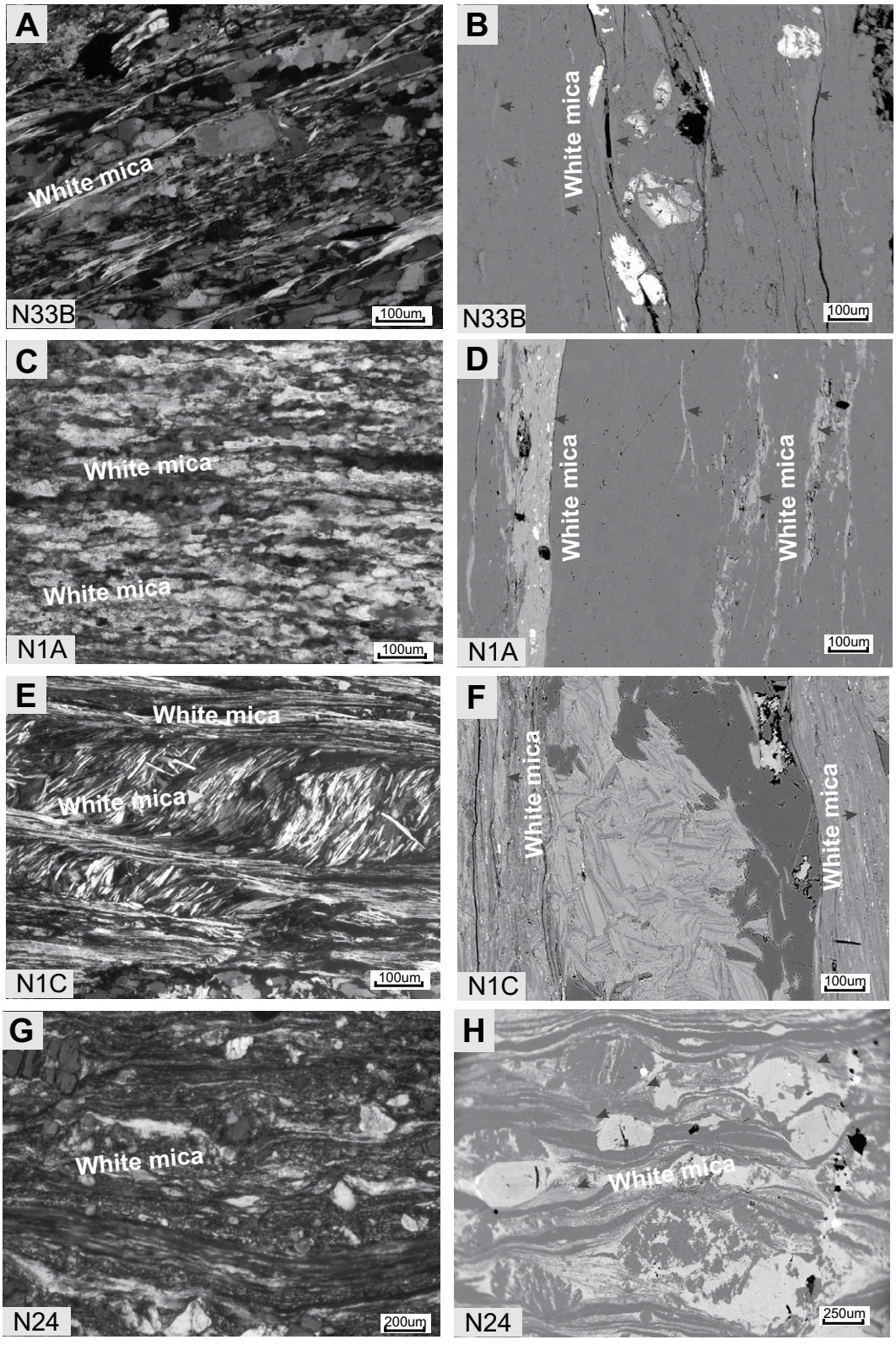

Figure 11. Microfabrics of strongly retrogressed samples containing white mica used for $^{40}Ar/^{39}Ar$ dating.

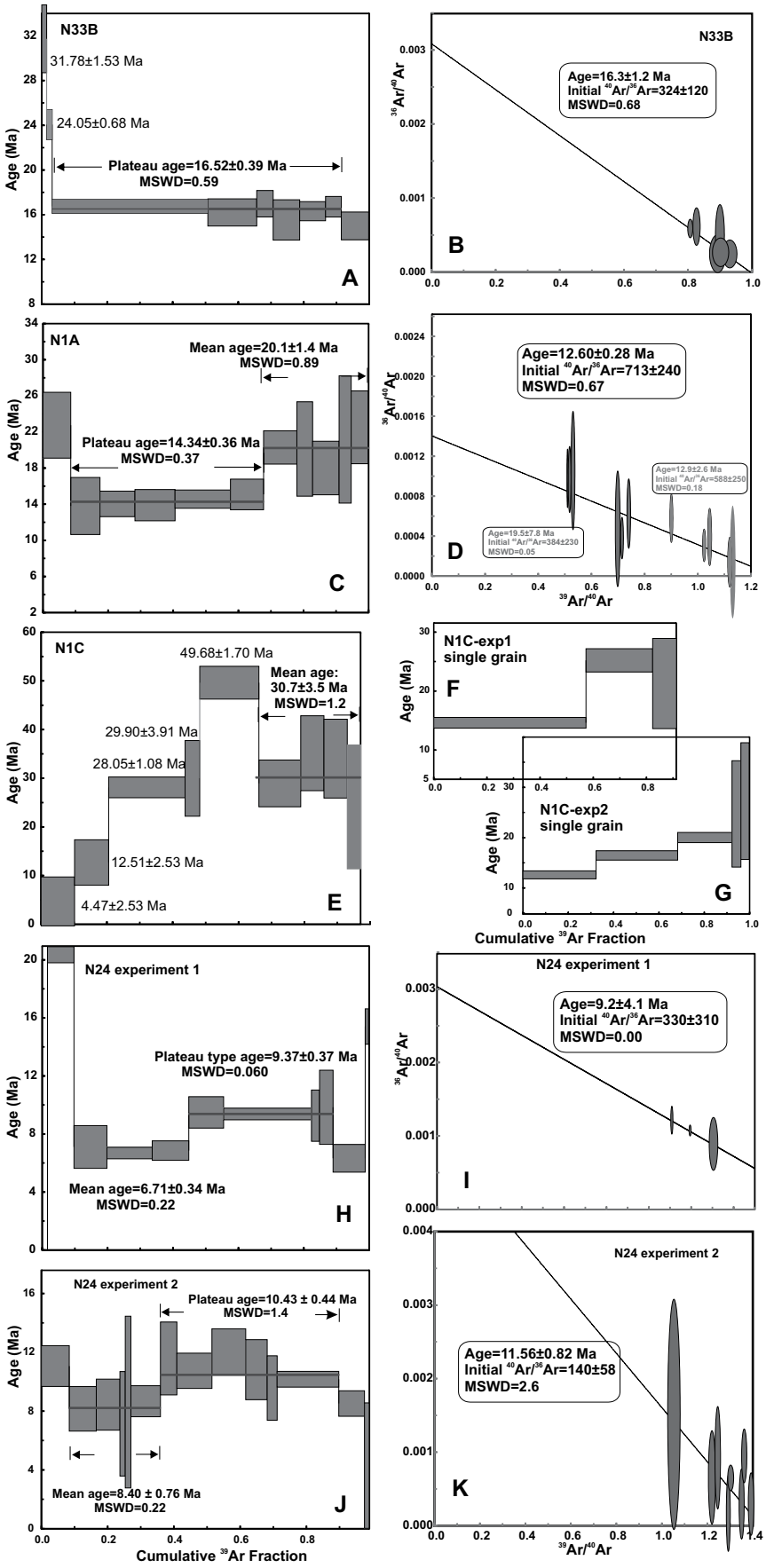

Figure 12. $^{40}Ar/^{39}Ar$ release patterns and isotopic inversion diagrams for white mica separates from strongly retrogressed samples. MSWD—mean square of weighted deviates.

means that this sample includes a variety of age populations with old ages and two younger populations, which is the same as the isochrones of the nearby sample N1A at 12.6 ± 0.28 Ma and 20.1 ± 1.4 Ma. Together, the experiments show a mixture of inherited high-pressure grains (38.3 ± 4.2 Ma) and of newly recrystallized grains during shearing. The age of the latter is reasonably constrained by Ar loss between 13.9 ± 0.9 Ma and 11.9 ± 0.8 Ma.

Sample N24 is a mylonitic aplite gneiss from the northern part close the Naxos-Paros detachment. Microstructures show strong plastic deformation of the main mineral phases (e.g., quartz, white mica, feldspar) in the sample. Sheared porphyroclasts and recrystallized white mica are surround feldspar porphyroclasts. Two experiments on multiple grains were performed. White mica from sample N24-exp1 gave a mean age of 6.71 ± 0.34 Ma for steps 2–4 and a plateau age of 9.37 ± 0.37 Ma (steps 5–8, 50% of ^{39}Ar released; Fig. 12H). Isotope inversion resulted in an age of 9.2 ± 4.1 Ma (with a $^{40}Ar/^{36}Ar$ initial value of 330 ± 310 Ma; Fig. 12I). We consider the plateau age of 9.37 ± 0.37 Ma to be geologically significant and to date the time of shearing. The largest white mica grains were selected to perform another experiment on sample N24. The experiment N24-exp2 gave a somewhat scattered Ar release pattern, which allowed the calculation of a mean age of 8.40 ± 0.76 Ma (steps 2–6) and a plateau age of 10.43 ± 0.44 Ma (steps 7–12; Fig. 12J). Isotope inversion resulted in an age of 11.56 ± 0.82 Ma (with a $^{40}Ar/^{36}Ar$ initial value of 140 ± 58 Ma; Fig. 12K). We think that the results of both experiments are geologically meaningful, showing shearing, which started at 10.43 ± 0.44 Ma and possibly lasted until 6.71 ± 0.34 Ma.

DISCUSSION

Impact of Retrogression on Microfabrics

As described already, in the Naxos metamorphic core complex, retrogression has been documented along some local shear zones (e.g., Urai et al., 1990), but regional retrogression is still rarely discussed in more detail. It is especially noteworthy that the presence of low-temperature overprinted fabrics in these localities indicates that retrogression was not only restricted to the boundary shear zone of Naxos

(e.g., Cao et al., 2013a), but it also affected large domains of the entire metamorphic sequence of the Naxos metamorphic core complex. The metamorphic rocks show abundant microstructures that can be readily related to retrograde processes. These processes include development of fine quartz grains by bulging recrystallization, brittle deformation of feldspar, coarse calcite grains with irregular boundaries and thin mechanical twins, homogeneous grain-size reduction of biotite, and the occurrence of discrete microshear zones with fine-grained white mica, which relate to the regional deformation/exhumation. Displacement and/or pull-apart of fractured feldspar porphyroclasts in the quartz and biotite matrix indicate that shearing continued under low-temperature (lower greenschist-facies) conditions. Textures of quartz-ofeldspathic mylonitic gneisses and marbles are consistent with extensive late retrogressive activity. The compositions of muscovite and chlorite reflect a diverse origin and time of growth. Conspicuously, inherited grains from M1 and M2 stages of metamorphism are often preserved in mylonites. The presence of secondary chlorite and albite in boudins and shear bands, and the absence of annealing of the high-pressure mineralogy indicate that later stages of deformation also occurred at relatively low *P-T* conditions. The orthogneisses and aplitic dikes may be explained by a sequence in which early high-temperature mylonitic fabrics and microstructures were overprinted by semibrittle to brittle adjustments during exhumation through the ductile-brittle transition. Shear sense criteria in these rocks indicate top-to-the-N sense of motion, as documented in other parts of the island in relation to extension (Urai et al.,1990; Buick, 1991a, 1991b), but late shear bands showing top-to-the-S sense of shear are also well developed (Avigad, 1998).

The Naxos metamorphic core complex can be interpreted to have developed finally under retrogressive conditions so that the zone of strongest shearing narrowed toward the margins of the Naxos Granite, suggesting that strain localization occurred during cooling of the granitic rocks. Within the Naxos metamorphic core complex, the interior is also strongly affected by retrogression. Retrogression in the migmatite core occurred by inflow of meteoric hydrous fluids along approximately E-W–trending quartz veins, for which Siebenaller et al. (2013) found *P-T* conditions at 250 °C and 80 MPa. Chlorites within mylonitic phyllites are found to lose stability even within sub-greenschist-facies metamorphic conditions during shearing, and a succession of chlorite formation from higher to lower temperatures can be found. A reason could be the interaction of older mineral assemblages with hydrous fluids, possibly hydrothermal fluids along the zone of shearing and retrogression during brittle-ductile transition. This is believed to reset the chemical composition of feldspar, chlorite, and white mica. We therefore take the temperatures of the chlorite thermometry as approximate values of the final stages of retrogression, and these values are consistent with temperatures found in the fluid inclusion study of Siebenaller et al. (2013). The data show that earlier microfabrics such as those in microlithons (type 1) yield higher temperatures than the subsequent sheared chlorites (type 2). If the temperatures are approximately correct, this would suggest that ductile shear in phyllosilicate-rich rocks and marbles possibly occurred at sub-greenschist-facies metamorphic conditions (at temperature ranging from 320 °C to 215 °C).

Retrogression and Geological Significance of the Melanes Shear Zone

The W-dipping Melanes zone is a retrogressive shear zone, along which amphibolite-grade metamorphic rocks were retrogressed during NNE-directed shearing. The ductile deformation of the metamorphic rocks in the Melanes shear zone was accompanied by extreme grain-size reduction of minerals during the retrogressive event. An estimate of the temperature conditions during retrogressive deformation can be inferred by the features of the deformed behavior of the minerals in shear zones (Simpson, 1985). The temperature is also estimated, by the chlorite thermometry, at low-grade conditions within marble (300–400 °C). The Melanes shear zone forms the eastern limb of a synform between the Naxos metamorphic core complex in the east and the Naxos Granite in the west, in which the bedding of Lower Miocene clastic rocks is in part in a nearly subvertical position. Consequently, the Naxos-Paros detachment fault, including the Melanes shear zone, seems to have been folded after deposition and after intrusion of the Naxos Granite by a major phase of E-W shortening, as already mentioned. For a few Cycladic islands, such late-stage E-W shortening was also previously postulated by Urai et al. (1990), Avigad et al. (2001), and Marsellos et al. (2010).

Timing of Deformation with Respect to Retrogression within the Naxos Metamorphic Core Complex

The relative succession recorded by microstructures and fabrics and the $^{40}Ar/^{39}Ar$ white mica ages allow dating of these events for the whole metamorphic core complex. Isotopic exchange in recrystallized minerals is controlled by the relative importance of microstructure development, including grain-size reduction (e.g., Mulch and Cosca, 2004). White mica can grow over a variety of time scales under a large range of metamorphic conditions (e.g., Mulch and Cosca, 2004). Retrogressive mylonitization within the Naxos metamorphic core complex occurred under greenschist-facies conditions during exhumation. The new data from fine-grained sheared rocks also reveal that some earlier-formed, phengite-rich white mica grains possibly remained compositionally stable, although subsequent shearing and other muscovite-rich grains formed new microstructures. These fine-grained white micas were well developed in the mylonitic foliation and in shear bands during the retrogressive deformation (post-M2) evidenced by microstructural and petrographic observations.

Phengites of the M1 metamorphic stage underwent deformation during the interval between the M1 and M2 metamorphic stages. However, the effect of deformation on the Ar isotopic ages seems to have been different in different samples. Instead, crystallization of muscovite during the M2 metamorphism at the expense of phengite appears to be the most important process for resetting of the argon isotopic system. From the results of white mica $^{40}Ar/^{39}Ar$ dating, we found three reasonably constrained ages associated with retrogressive growth of white mica within the Naxos metamorphic core complex: (1) A plateau age of 16.52 ± 0.39 Ma in a shear zone in the southern part is interpreted as the formation age of a retrogressive shear zone overprinting earlier fabrics. (2) Another plateau age of 14.34 ± 0.36 Ma and evidence for Ar loss of older grains between 13.9 ± 0.9 Ma and 11.9 ± 0.8 Ma indicate motion along in the Moutsounas shear zone and directly date shearing at the upper margin of the Naxos metamorphic core complex, although some uncertainty remains. This is in agreement with the stratigraphic evidence given by overlying sediments from Naxos and Paros, which range in age between 11 and 5 Ma (Bargnesi et al., 2013). (3) Finally, very young plateau ages of 10.43 ± 0.44 Ma to 8.40 ± 0.76 Ma were found in the northern part of the Naxos metamorphic core complex, which is consistent with the youngest time of ductile shear deformation along the Naxos-Paros ductile normal fault. The age is close to cooling ages also recorded in nearby (U-Th)/He zircon and apatite fission-track ages of ca. 12 Ma and ca. 9 Ma (Seward et al., 2009; Brichau et al., 2006). This implies rapid cooling and possibly localized shear heating affecting white mica during recrystallization by thermally resetting the argon isotopic system through loss of radiogenic argon. A high

geothermal gradient of 55 °C/km at hydrostatic pressure was assumed for this final stage of exhumation (Siebenaller et al., 2013), supporting the assumption of rapid cooling.

Retrogression within the Granodiorite (Naxos Granite)

Shear deformation within the Naxos metamorphic core complex continued after emplacement of bodies of the Naxos granodiorite to the west (e.g., Faure et al., 1991; John and Howard, 1995). The data presented herein suggest that the penetrative microstructural and fabric development in the granodiorite at eastern margins of the Naxos Granite was associated with early N-directed shearing at relatively high-grade temperature conditions. The calculated temperature of sample N72 is in the range from 661 °C to 583 °C, and the average is 621 ± 19 °C (Table DR1 [see footnote 1]). Since these granitic rocks were not metamorphosed, this deformation phase could have developed during cooling of the granodiorite. Ductile-brittle reactivation, associated with low-temperature hydrothermal alteration and formation of pervasive chlorite, appears to have occurred late in the deformation history of the granodiorite, indicating that the deformation occurred within the greenschist facies, as supported by results of the chlorite thermometry calculations. Consequently, microstructures reflect cooling of the granodioritic rocks from the ductile to semiductile (ductile-brittle) regime (e.g., Sibson, 1977; Shimamoto, 1989) during retrogression.

Keay et al. (2001) and Bolhar et al. (2010) found that the I-type Naxos Granite body crystallized episodically between 13 and 11 Ma. Note that the ages of retrogression within the Naxos Granite are, therefore, significantly younger than the age of motion along the Moutsounas shear zone. This observation was attributed to a protracted history involving initial partial melting at deeper crustal levels, followed by crystallization and cooling at progressively shallower crustal levels. All zircon and apatite fission-track ages of the Naxos metamorphic core complex and the Naxos Granite range from 11.8 ± 0.8 to 9.7 ± 0.8 Ma and 11.2 ± 1.6 to 8.2 ± 1.2 Ma, respectively, and consistently decrease northward in the direction of hanging-wall transport (Hejl et al., 2002; Brichau et al., 2006; Andriessen, 1991), but Seward et al. (2009) could not find this trend. Brichau et al. (2006) interpreted their results to support the scenario of an identical fault dip and a constant or slightly accelerating slip rate of ~6–8 km/m.y. on the Naxos-Paros extensional fault system across the brittle-ductile transition, which separated the metamorphic core complex from the overlying unit during exhumation. A rolling hinge top-to-the-N displacement was proposed in recent models (Brichau et al., 2006; Jolivet et al., 2010). Interestingly, we can distinguish two stages of tilting. In the south, the intrusional relationships between granodiorite of the Naxos Granite body and the Naxos metamorphic core complex are exposed, which formed during intrusion of the granodiorite between 13 and 11 Ma, and, in the north, a synform with Lower Miocene sedimentary rocks is observed. Consequently, the southern part is from a deeper level, implying tilting to the north. This is in contrast to cooling ages of Brichau et al. (2006), which imply an earlier age of cooling between ca. 11 and 8 Ma in the south and consequently top-to-the-S tilting according to their rolling hinge model.

Southward Shift of Retrogression in the Attic-Cycladic Belt

Retrogression, generally overprinting high-pressure rocks, is a common phenomenon in the Attic-Cycladic belt (Fig. 1B). For retrogression, we also recognize a trend from older ages of 29–21 Ma in the north to 11–8 Ma in the south (Fig. 1B). Again, Naxos has in intermediate position but shows a wide temporal range of retrogression within the Naxos metamorphic core complex, consistent with retrogressive deformation within other metamorphic core complexes of the Aegean Sea (Fig. 1B). We interpret these long temporal ranges of retrogression to reflect outward southwestward retreat of subduction and, therefore, sequential activation of major detachment zones (Ring et al., 2010).

Generalized Model for Retrogression: Implications for Exhumation

An understanding of the retrogression history of the Naxos metamorphic core complex has helped in deciphering the metamorphic scheme, including the *P-T* path and exhumation processes of metamorphic rocks. This reequilibration is facilitated by information from fluid-rock interaction, and new mineral assemblages that are often developed in discrete zones of extensive retrogression during ductile-brittle transition (e.g., Kreulen, 1980; Cartwright and Buick, 1995; Buick and Holland, 1989; Cao et al., 2013a, 2013b) and inflow through subvertical veins (Siebenaller et al., 2013). During low-temperature retrogression, microshear zones appear to have been zones of more focused and discrete deformation and fluid-rock interaction in comparison to earlier high-temperature retrogression. In most structural settings, dynamic retrogression is related to the brittle-ductile transition zone (e.g., Michibayashi and Masuda, 1993), although retrogression in much deeper structural levels could occur, e.g., the amphibolitization of water-free granulite- or eclogite-facies mineral assemblages (e.g., El-Shazly and Sisson, 1999; Xu et al., 2009). At the brittle-ductile transition, retrogressed sheared rocks are most common, and fluid flow is proven by precipitation of minerals such as chlorite along the overlying cataclastic carapace. This also involves leaching of elements and minerals mostly from the footwall. The sources of hydrous fluids could be from three basic sources, which could be possibly distinguished by fluid inclusion and stable isotope (hydrogen, oxygen) studies (Siebenaller et al., 2013). These sources include: (1) descending meteoric water (and possibly seawater) from sedimentary basins or the surface (e.g., Yardley et al., 2000), which infiltrates along brittle normal faults to depth, and (2) ascending magmatic-induced hydrous fluid flow during exhumation of metamorphic rocks, e.g., from synextensional granites (e.g., Zong et al., 2010). (3) The higher-than-normal heat flow also might trigger metamorphic dehydration reactions at depth, like decomposition of chlorite, muscovite, or biotite, which then yields a significant amount of uprising hydrous metamorphic fluids. The flow of hydrous fluids would trigger a number of processes along the zone of shearing and retrogression during ductile-brittle transition, among which the lowering of the shear stress of rock-constituting minerals like quartz (Tullis and Yund, 1989; Chernak et al., 2009), sericitization of feldspar, and chloritization are the most important ones. In the case of the Naxos metamorphic core complex and the Naxos Granite, fluids could be expected to have derived from all three sources (see also Siebenaller et al., 2013): metamorphic dehydration reactions at depth, magmatic fluids from granite intrusions, and meteoric fluids from the hanging-wall unit. Because of the long duration of the metamorphic processes, some continuity of retrogression can be expected between ca. 16 and 9 Ma.

In Figure 13, we describe a generalized model for retrogression related to late-stage ductile-brittle transition, when the metamorphic core complex reached shallow crustal levels during exhumation. The model is based on the geodynamic, structural, and petrologic conditions of the Naxos metamorphic core complex, but it could be applied to other geodynamic settings in which extension prevails. The cooling of the exhuming metamorphic core complex results in ascent of the brittle-ductile transition zone to higher structural levels by cooling and exhumation of formerly deeply buried rocks. In these settings, subvertical gashes and veins can be found, and some of these veins are filled

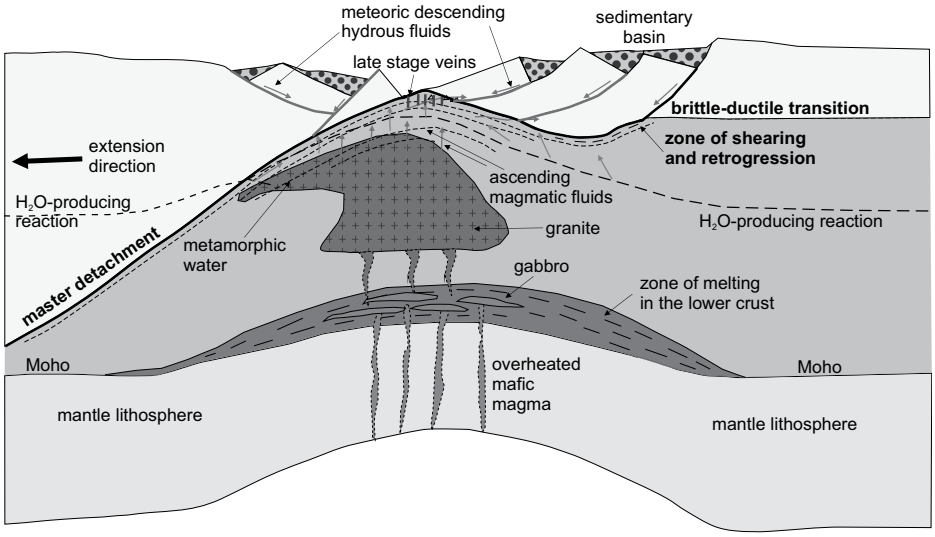

Figure 13. General tectonic model of retrogression related to late-stage ductile-brittle transition, when the metamorphic core complex reached shallow crustal levels during exhumation.

by minerals precipitated from ascending and descending fluids. It is generally at the level of the veins where ascending fluids are overheated with respect to the temperature of the country rocks, representing, therefore, hydrothermal fluids (Scott et al., 2015). In such cases, these fluids can also transform the country rocks by static retrogression. This may be generally the case when these veinlets and veins are generally undeformed and occur in a late stage of the structural succession, as in the case of the Mykonos (Menant et al., 2013) and Sifnos metamorphic core complexes (Neubauer, 2005). Note that such veins are often also mineralized with ore minerals.

In summary, all these minerals lower the differential stress along the zone of shearing, retrogression, and faults and lead finally to shear concentration within such zones at the ductile-brittle transition. This represents and provides a positive feedback mechanism for faulting and stabilization of retrogression immediately below the brittle-ductile transition zone during exhumation of metamorphic core complexes.

CONCLUSIONS

The following major conclusions can be drawn from this study:

(1) Microstructural and textural analysis of samples and field observations reveals that there is variable retrogression within the detachment shear zone. Retrogression even pervasively affected significant portions of the migmatite-grade metamorphic core and remnant high-pressure areas. There, retrogression led to pervasive formation of new fabrics within greenschist- and sub-greenschist-facies metamorphic conditions during the exhumation of the Naxos metamorphic core complex.

(2) Detailed analysis of the microstructure, composition, and $^{40}Ar/^{39}Ar$ dating of synkinematic white micas constrains retrogressive deformation conditions and change of fabrics within and at the top of the Naxos metamorphic core complex and Naxos Granite. The thermochronologic data record retrogression in late Miocene times (ca. 16.52 ± 0.39 Ma to 8.40 ± 0.76 Ma), consistent with final exhumation of the Naxos metamorphic core complex.

(3) Retrogressive microstructures, low-temperature calcite fabrics in marbles, and chloritization in metapelites (at temperatures of ~350–130 °C) in the Naxos metamorphic core complex core mainly developed during late-stage E-W shortening and folding. The lower-temperature group could be tentatively interpreted to be the result either of a late-stage hydrothermal overprint related to granite/granodiorite intrusions or inflow of meteoric water. The flow of hydrous fluids resulted in resetting of fabrics.

(4) The wide temporal range of retrogression within the Naxos metamorphic core complex may be consistent with retrogressive deformation within other metamorphic core complexes of the Aegean Sea. We interpret this long temporal range to reflect outward southwestward retreat of subduction and therefore sequential activation of major detachment zones.

APPENDIX: ANALYTICAL METHODS

Backscattered Electron Diffraction Method

Crystallographic preferred orientations (CPOs) were measured using a backscattered electron diffraction (BSED) detector mounted on a tungsten filament Hitachi S-3400N-II scanning electron microscope (SEM) at the China University of Geosciences, Beijing (Liu et al., 2012). Detailed optical microstructural observations and CPO analysis were conducted on thin sections. All thin sections were cut parallel to the kinematic *x*-*z* plane (where *x* is parallel to lineation, *y* is parallel to foliation and normal to lineation, and *z* is normal to foliation). Highly polished thin sections were prepared without cover and polished using a colloidal silica suspension with a particle size of 500 nm for 1–3 h. Thin sections were put in the SEM chamber at a 70° tilt angle with the rock lineation (structural *x* reference direction) parallel to the SEM *x* axis. The BSE patterns were acquired at a low acceleration voltage of 15 kV and a beam working distance of ~18–20 mm. Conducting resin tapes attached to the sample surface surrounding the measurement area were used to reduce charging effects. The BSED data acquisition was done using both point scan and mapping modes. Indexing was accepted when at least six detected Kikuchi bands matched with those in the standard reflector file for the analyzed mineral phases, and indexed points with a mean angular deviation (MAD) larger than 1.2 (between detached and simulated patterns) were eliminated to avoid suspicious indexing. BSED analysis was completed using the HKL Channel 5 software package. Pole figures were plotted in lower-hemisphere equal-area stereographic diagrams with the trace of the mylonitic foliation (S) and the stretching lineation (L) as reference directions. Systematic misindexing was noted in automated orientation maps, and such data were replaced by zero solution pixels. A detailed description of the BSED technique can be found in, e.g., Prior et al. (1996).

Electron Microprobe Analysis (EPMA) Methodology

EMPA of the mineral chemistry of minerals (white mica, two feldspars, chlorite, garnet, biotite) were carried out on a JEOL electron microprobe (JXA-8600) at the Department Geography and Geology, University of Salzburg, using a wavelength dispersive system. We used an acceleration voltage of 15 kV and a sample current of 40 nA. Natural and synthetic mineral standards were used to calibrate the microprobe, and raw data were reduced using standard ZAF correction. The detection limits (2σ) for the elements are: Si = 0.06 wt%, Al = 0.04 wt%, and Na, K, Mg, Mn, and Fe = 0.025 wt%.

$^{40}Ar/^{39}Ar$ Method

The $^{40}Ar/^{39}Ar$ analytical techniques largely follow descriptions given in Handler et al. (2004) and Rieser et al. (2006). Preparation of the samples before and after irradiation, $^{40}Ar/^{39}Ar$ analyses, and age calculations were carried out at the ARGONAUT Laboratory of the Geology Division at the University of Salzburg. The mineral separates were obtained by crushing hand-sized samples and sieving through 200–355 µm fractions. They were further purified by washing with deionized water. Mineral concentrates were packed in aluminum foil and placed in quartz vials. For calculation of the *J*-values, flux monitors were placed between each 4 or 5 unknown samples. The sealed quartz vials were irradiated in the Rez reactor (Prague, Czech Republic) for 16 h. Correction factors for interfering isotopes were calculated from 10 analyses of two Ca-glass samples and 22 analyses of two pure K-glass samples, and they are: $^{36}Ar/^{37}Ar(Ca) = 0.00022500$, $^{39}Ar/^{37}Ar(Ca) = 0.00061400$, and $^{40}Ar/^{39}Ar(K) = 0.026600$. Variation in the flux of neutrons was monitored with the DRA1 sanidine standard, for which a $^{40}Ar/^{39}Ar$ plateau age of 25.03 ± 0.05 Ma was origi-

nally reported (Wijbrans et al., 1995). Here, we used the revised value of 25.26 ± 0.05 Ma (van Hinsbergen et al., 2008). The $^{40}Ar/^{39}Ar$ analyses were carried out using an ultrahigh-vacuum Ar-extraction line equipped with a combined infrared (IR) laser system, and a VG-ISOTECHTMNG3600 mass spectrometer.

Stepwise heating analyses of samples were performed using a defocused (1.5 mm diameter) 25 W CO_2-IR laser operating in Tem00 mode at wavelengths between 10.57 and 10.63 µm. Gas admittance and pumping of the mass spectrometer and the Ar extraction line were computer-controlled using pneumatic valves. The NG3600 is an 18-cm-radius 60° extended geometry instrument, equipped with a bright Nier-type source operated at 4.5 kV. Measurements were performed on an axial electron multiplier in static mode with peak jumping, and the stability of the magnet was controlled by a Hall probe? For each increment, the intensities of ^{36}Ar, ^{37}Ar, ^{38}Ar, ^{39}Ar, and ^{40}Ar were measured, and the baseline readings on mass 34.5 were automatically subtracted. Intensities of the peaks were back-extrapolated over 16 measured intensities to the time of gas admittance either by a straight line or a curved fit, depending on intensity and type of pattern of the evolving gas. Intensities were corrected for system blanks, background, post-irradiation decay of ^{37}Ar, and interfering isotopes. Isotopic ratios, ages, and errors for individual steps were calculated following suggestions by McDougall and Harrison (1999) and Scaillet (2000) using decay factors reported by Steiger and Jäger (1977). Definition and calculation of plateau ages were carried out using ISOPLOT/EX (Ludwig, 2001).

ACKNOWLEDGMENTS

We gratefully acknowledge thorough and valuable comments by Uwe Ring, Neill Mancktelow, Stefano Mazzoli, Anthony J. Barber, Christian Koeberl, and Enrico Tavarnelli that helped us improve the paper. We acknowledge support from Austrian Science Foundation (FWF) grants M-1343 and P28313-N29, National Natural Science Foundation of China grant 41472188, and grant MSFGPMR201406 from the MOST Special Fund from the State Key Laboratory of Geological Processes and Mineral Resources, China University of Geosciences (Wuhan).

REFERENCES CITED

Altherr, R., Kreuzer, H., Wendt, I., Lenz, H., Wagner, G.A., Keller, J., Harre, W., and Hohndorf, A., 1982, A late Oligocene/early Miocene high temperature belt in the Attic-Cycladic crystalline complex (SE Pelagonian, Greece): Geologisches Jahrbuch, v. 23, p. 97–164.

Anderson, J.L., 1996, Status of thermobarometry in granitic batholiths: Transactions of the Royal Society of Edinburgh–Earth Sciences, v. 87, p. 125–138, doi:10.1017/S0263593300006544.

Andriessen, P.A.M., 1991, K-Ar and Rb-Sr age determinations on micas of impure marbles of Naxos, Greece: The influence of metamorphic fluids and lithology on the blocking temperature: Schweizerische Mineralogische und Petrographische Mitteilungen, v. 71, p. 89–99.

Andriessen, P.A.M., Boelrijk, N.A.I.M., Hebeda, E.H., Priem, H.N.A., Verdurmen, E.A.T., and Verschure, R.H., 1979, Dating the events of metamorphism and granitic magmatism in the Alpine orogen of Naxos (Cyclades Greece): Contributions to Mineralogy and Petrology, v. 69, p. 215–225, doi:10.1007/BF00372323.

Andriessen, P.A.M., Banga, G., and Hebeda, E.H., 1987, Isotopic age study of pre-Alpine rocks in the basal units on Naxos, Sikinos and Ios, Greek Cyclades: Geologie en Mijnbouw, v. 66, p. 3–14.

Avigad, D., 1998, High-pressure metamorphism and cooling on SE Naxos (Cyclades, Greece): European Journal of Mineralogy, v. 10, p. 1309–1319, doi:10.1127/ejm/10/6/1309.

Avigad, D., and Garfunkel, Z., 1991, Uplift and exhumation of high-pressure metamorphic terrains: The example of the Cycladic blueschist belt (Aegean Sea): Tectonophysics, v. 188, p. 357–372, doi:10.1016/0040-1951(91)90464-4.

Avigad, D., Ziv, A., and Garfunkel, Z., 2001, Ductile and brittle shortening, extension-parallel folds and maintenance of crustal thickness in the central Aegean (Cyclades): Tectonics, v. 20, p. 277–287, doi:10.1029/2000TC001190.

Bargnesi, E.A., Stockli, D., Mancktelow, N., and Soukis, M., 2013, Miocene core complex development and coeval supradetachment basin evolution of Paros, Greece, insights from (U-Th)/He thermochronometry: Tectonophysics, v. 595–596, p. 165–182, doi:10.1016/j.tecto.2012.07.015.

Böger, H., 1983, Stratigraphische und tektonische Verknuepfungen kontinentaler Sedimente des Neogens im Aegais-Raum: Geologische Rundschau, v. 72, p. 771–813, doi:10.1007/BF01848344.

Bolhar, R., Ring, U., and Allen, C.M., 2010, An integrated zircon geochronological and geochemical investigation into the Miocene plutonic evolution of the Cyclades, Aegean Sea, Greece: Part 1. Geochronology: Contributions to Mineralogy and Petrology, v. 160, p. 719–742, doi:10.1007/s00410-010-0504-4.

Brichau, S., Ring, U., Ketcham, R.A., and Carter, A., 2006, Constraining the long-term evolution of the slip rate for a major extensional fault system in the central Aegean, Greece, using thermochronology: Earth and Planetary Science Letters, v. 241, p. 293–306, doi:10.1016/j.epsl.2005.09.065.

Brichau, S., Thomson, S., and Ring, U., 2010, Thermochronometric constraints on the tectonic evolution of the Serifos detachment, Aegean Sea, Greece: International Journal of Earth Sciences, v. 99, p. 379–393, doi:10.1007/s00531-008-0386-0.

Bröcker, M., Kreuzer, H., Matthews, A., and Okrusch, M., 1993, $^{40}Ar/^{39}Ar$ and oxygen isotope studies of polymetamorphism from Tinos Island, Cycladic blueschist belt: Journal of Metamorphic Geology, v. 11, p. 223–240, doi:10.1111/j.1525-1314.1993.tb00144.x.

Bröcker, M., Bieling, D., Hacker, B., and Gans, P., 2004, High-Si phengite records the time of greenschist facies overprinting: Implications for models suggesting megadetachments in the Aegean Sea: Journal of Metamorphic Geology, v. 22, p. 427–442, doi:10.1111/j.1525-1314.2004.00524.x.

Bröcker, M., Baldwin, S., and Arkudas, R., 2013, The geological significance of $^{40}Ar/^{39}Ar$ and Rb-Sr white mica ages from Syros and Sifnos, Greece: A record of continuous (re)crystallization during exhumation?: Journal of Metamorphic Geology, v. 31, p. 629–646, doi:10.1111/jmg.12037.

Buick, I.S., 1991a, The late Alpine evolution of an extensional shear zone, Naxos, Greece: Journal of the Geological Society of London, v. 148, p. 93–103, doi:10.1144/gsjgs.148.1.0093.

Buick, I.S., 1991b, Mylonite fabric development on Naxos, Greece: Journal of Structural Geology, v. 13, p. 643–655, doi:10.1016/0191-8141(91)90027-G.

Buick, I.S., and Holland, T.J.B., 1989, The *P-T-t* path associated with crustal extension, *in* Daly, J.S., Cliff, R.A., and Yardley, B.W.D., eds., Evolution of Metamorphic Belts: Geological Society of London Special Publication 43, p. 365–369, doi:10.1144/GSL.SP.1989.043.01.32.

Cao, S., Neubauer, F., Bernroider, M., and Liu, J., 2013a, The lateral boundary of a metamorphic core complex: The Moutsounas shear zone on Naxos, Cyclades, Greece: Journal of Structural Geology, v. 54, p. 103–128, doi:10.1016/j.jsg.2013.07.002.

Cao, S., Neubauer, F., Bernroider, M., Liu, J., and Genser, J., 2013b, Structures, microfabrics and textures of the Cordilleran-type Rechnitz metamorphic core complex, eastern Alps: Tectonophysics, v. 608, p. 1201–1225, doi:10.1016/j.tecto.2013.06.025.

Cartwright, I., and Buick, I.S., 1995, Formation of wollastonite-bearing marbles during late-regional metamorphic channeled fluid flow in the Upper Calcsilicate Unit, Reynolds Rang Group, central Australia: Journal of Metamorphic Geology, v. 13, p. 397–417, doi:10.1111/j.1525-1314.1995.tb00228.x.

Cathelineau, M., 1988, Cation site occupancy in chlorites and illites as a function of temperature: Clay Minerals, v. 23, p. 471–485, doi:10.1180/claymin.1988.023.4.13.

Cathelineau, M., and Nieva, D., 1985, A chlorite solid solution geothermometer. The Los Azufres (Mexico) geothermal system: Contributions to Mineralogy and Petrology, v. 91, p. 235–244, doi:10.1007/BF00413350.

Chernak, L.J., Hirth, G., Selverstone, J., and Tullis, J., 2009, Effect of aqueous and carbonic fluids on the dislocation creep strength of quartz: Journal of Geophysical Research–Solid Earth, v. 114, p. B04201, doi:10.1029/2008JB005884.

Cossette, É., Schneider, D.A., Warren, C.J., and Grasemann, B., 2015, Lithological, rheological, and fluid infiltration control on $^{40}Ar/^{39}Ar$ ages in polydeformed rocks from the West Cycladic detachment system, Greece: Lithosphere (in press), doi:10.1130/L416.1.

Duchêne, S., Aissa, R., and Vanderhaeghe, O., 2006, Pressure-temperature-time evolution of metamorphic rocks from Naxos (Cyclades, Greece): Constraints from thermobarometry and Rb/Sr dating: Geodinamica Acta, v. 19, p. 301–321, doi:10.3166/ga.19.301-321.

Dunlap, W., 1997, Neocrystallization or cooling? $^{40}Ar/^{39}Ar$ ages of white micas from low-grade mylonites: Chemical Geology, v. 143, p. 181–203, doi:10.1016/S0009-2541(97)00113-7.

El-Shazly, A.K., and Sisson, V.B., 1999, Retrograde evolution of eclogite facies rocks from NE Oman: Evidence from fluid inclusions and petrological data: Chemical Geology, v. 154, p. 193–223, doi:10.1016/S0009-2541(98)00132-6.

Faure, M., Bonneau, M., and Pons, J., 1991, Ductile deformation and syntectonic granite emplacement during the late Miocene extension of the Aegean (Greece): Bulletin de la Société Géologique de France, v. 162, p. 3–11.

Ferrill, D.A., Morris, A.P., Evans, M.A., Burkhard, M., Groshong, R.H., and Onasch, C.M., 2004, Calcite twin morphology: A low-temperature deformation geothermometer: Journal of Structural Geology, v. 26, p. 1521–1529, doi:10.1016/j.jsg.2003.11.028.

Gautier, P., Brun, J.P., and Jolivet, L., 1993, Structure and kinematics of Upper Cenozoic extensional detachment on Naxos and Paros (Cyclades Islands, Greece): Tectonics, v. 12, p. 1180–1194, doi:10.1029/93TC01131.

Gébelin, A., Teyssier, C., Heizler, M., and Mulch, A., 2014, Meteoric water circulation in a rolling-hinge detachment system (northern Snake Range core complex, Nevada): Geological Society of America Bulletin, v. 127, no. 1–2, p. 149–161, doi:10.1130/B31063.1.

Grasemann, B., Schneider, D.A., Stöckli, D.F., and Iglseder, C., 2012, Miocene bivergent crustal extension in the Aegean: Evidence from the western Cyclades (Greece): Lithosphere, v. 4, p. 23–39, doi:10.1130/L164.1.

Handler, R., Velichkova, S.H., Neubauer, F., and Ivanov, Z., 2004, $^{40}Ar/^{39}Ar$ age constraints on the timing of the formation of Cu-Au deposits in the Panagyurishte region, Bulgaria: Schweizerische Mineralogische und Petrographische Mitteilungen, Special issue GEODE-ABCD, v. 84, p. 119–132.

Harigane, Y., Michibayashi, K., and Ohara, Y., 2008, Shearing within lower crust during progressive retrogression: Structural analysis of gabbroic rocks from the Godzilla Mullion, an oceanic core complex in the Parece Vela backarc basin: Tectonophysics, v. 457, p. 183–196, doi:10.1016/j.tecto.2008.06.009.

Hejl, E., Riedl, H., and Weingartner, H., 2002, Post-plutonic unroofing and morphogenesis of the Attic-Cycladic complex (Aegean, Greece): Tectonophysics, v. 349, p. 37–56, doi:10.1016/S0040-1951(02)00045-8.

Hejl, E., Riedl, H., Soulakellis, N., Van De Haute, P., and Weingartner, H., 2003, Young Neogene tectonics and relief development on the Aegean islands of Naxos, Paros and Ios (Cyclades, Greece): Mitteilungen der Österreichischen Geologischen Gesellschaft, v. 93, p. 105–127.

Henjes-Kunst, F., Altherr, R., Kreuzer, H., and Hansen, B.T., 1988, Disturbed U-Th-Pb systematics of young zircons and uranothorites: The case of the Miocene Aegean granitoids (Greece): Chemical Geology, v. 73, p. 125–145.

Hetzel, R., Zwingmann, H., Mulch, A., Gessner, K., Akal, C., Hampel, A., Güngör, T., Petschick, R., Mikes, T., and Wedin, F., 2013, Spatiotemporal evolution of brittle normal faulting and fluid infiltration in detachment fault systems: A case study from the Menderes Massif, western Turkey: Tectonics, v. 32, p. 364–376, doi:10.1002/tect.20031.

Holland, T., and Blundy, J., 1994, Non-ideal interactions in calcic amphiboles and their bearing on amphibole-plagioclase thermometry: Contributions to Mineralogy and Petrology, v. 116, p. 433–447, doi:10.1007/BF00310910.

Huet, B., Labrousse, L., and Jolivet, L., 2009, Thrust or detachment? Exhumation processes in the Aegean: Insight from a field study on Ios (Cyclades, Greece): Tectonics, v. 28, p. TC3007, doi:10.1029/2008TC002397.

Huet, B., Pourhiet, L.L., Labrousse, L., Burov, E.B., and Jolivet, L., 2011, Formation of metamorphic core complex in inherited wedges: A thermomechanical modelling study: Earth and Planetary Science Letters, v. 309, p. 249–257, doi:10.1016/j.epsl.2011.07.004.

Huet, B., Labrousse, L., Monié, P., Malvoisin, B., and Jolivet, L., 2015, Coupled phengite ^{40}Ar-^{39}Ar geochronology and thermobarometry: *P-T-t* evolution of Andros Island (Cyclades, Greece): Geological Magazine, v. 152, p. 711–727, doi:10.1017/S0016756814000661.

Jacobshagen, V., 1986, Geologie von Griechenland: Berlin, Gebrüder Borntraeger, 636 p.

Jansen, J.B.H., 1973, Geological Map of Naxos: Athens, Institute of Geology and Mining Research, scale 1:25,000.

Jansen, J.B.H., 1977, The Geology of Naxos: Geology and Geophysical Research Volume 19: Athens, Greece, Institute of Geology and Mining Research, 100 p.

Jansen, J.B.H., and Schuiling, R.D., 1976, Metamorphism on Naxos: Petrology and geothermal gradients: American Journal of Science, v. 276, p. 1225–1253, doi:10.2475/ajs.276.10.1225.

John, B.E., and Howard, K.A., 1995, Rapid extension recorded by cooling-age patterns and brittle deformation, Naxos, Greece: Journal of Geophysical Research, v. 100, no. B6, p. 9969–9979, doi:10.1029/95JB00665.

Jolivet, L., and Faccenna, C., 2000, Mediterranean extension and the Africa-Eurasia collision: Tectonics, v. 19, p. 1095–1106, doi:10.1029/2000TC900018.

Jolivet, L., Faccenna, C., Goffé, B., Burov, E., and Agard, P., 2003, Subduction tectonics and exhumation of high-pressure metamorphic rocks in the Mediterranean orogens: American Journal of Science, v. 303, p. 353–409, doi:10.2475/ajs.303.5.353.

Jolivet, L., Lecomte, E., Huet, B., Denèle, Y., Lacombe, O., Labrousse, L., Le Pourhiet, L., and Mehl, C., 2010, The North Cycladic detachment system: Earth and Planetary Science Letters, v. 289, p. 87–104, doi:10.1016/j.epsl.2009.10.032.

Jolivet, L., Faccenna, C., Huet, B., Labrousse, L., Le Pourhiet, L., Lacombe, O., Lecompte, E., Burov, E., Denèle, Y., Brun, J.-P., Philippon, M., Paul, A., Salaün, G., Karabulut, T., Piromallo, C., Monié, P., Gueydan, F., Okay, A., Oberhänsli, R., Pourteau, A., Augier, R., Gadenne, L., and Driussi, O., 2012, Aegean tectonics: Strain localisation, slab tearing and trench retreat: Tectonophysics, v. 597–598, p. 1–33, doi:10.1016/j.tecto.2012.06.011.

Jowett, E.C., 1991, Fitting iron and magnesium into the hydrothermal chlorite geothermometer, *in* GAC/MAC/SEG Joint Annual Meeting Program with Abstracts: Toronto, Geological Association of Canada, v. 16, p. A62.

Kargaranbafghi, F., Neubauer, F., Genser, J., Faghih, A., and Kusky, T., 2012, Mesozoic to Eocene ductile deformation of western Central Iran: From Cimmerian collisional orogeny to Eocene exhumation: Tectonophysics, v. 564–565, p. 83–100, doi:10.1016/j.tecto.2012.06.017.

Keay, S., 1998, The Geological Evolution of the Cyclades, Greece: Constraints from SHRIMP U-Pb Geochronology [Ph.D. thesis]: Canberra, Australia, Australian National University, 341 p.

Keay, S., Lister, G., and Buick, I., 2001, The timing of partial melting, Barrovian metamorphism and granite intrusion in the Naxos metamorphic core complex, Cyclades, Aegean Sea, Greece: Tectonophysics, v. 342, p. 275–312, doi:10.1016/S0040-1951(01)00168-8.

Kirschner, D.L., Cosca, M.A., Masson, H., and Hunziker, J.C., 1996, Staircase ^{40}Ar/^{39}Ar spectra of fine-grained white mica; timing and duration of deformation and empirical constraints on argon diffusion: Geology, v. 24, p. 747–750, doi:10.1130/0091-7613(1996)024<0747:SAASOF>2.3.CO;2.

Koukouvelas, I.K., and Kokkalas, S., 2003, Emplacement of the Miocene west Naxos pluton (Aegean Sea, Greece): A structural study: Geological Magazine, v. 140, p. 45–61, doi:10.1017/S0016756802007094.

Krabbendam, M., Urai, J.J., and Vliet, L.J., 2003, Grain size stabilisation by dispersed graphite in a high-grade quartz mylonite: an example from Naxos (Greece): Journal of Structural Geology, v. 25, p. 855–866, doi:10.1016/S0191-8141(02)00086-X.

Kranidiotis, P., and MacLean, W.H., 1987, Systematics of chlorite alteration at the Phelps Dodge massive sulfide deposit, Matagami, Quebec: Economic Geology and the Bulletin of the Society of Economic Geologists, v. 82, p. 1898–1911, doi:10.2113/gsecongeo.82.7.1898.

Kreulen, R., 1980, CO_2-rich fluids during regional metamorphism on Naxos (Greece): Carbon isotopes and fluid inclusions: American Journal of Science, v. 280, p. 745–771, doi:10.2475/ajs.280.8.745.

Krohe, A., Mposkos, E., Diamantopoulos, A., and Kaouras, G., 2010, Formation of basins and mountain ranges in Attica (Greece): The role of Miocene to Recent low-angle normal detachment faults: Earth-Science Reviews, v. 98, p. 81–104, doi:10.1016/j.earscirev.2009.10.005.

Kruckenberg, S.C., Vanderhaeghe, O., Ferré, E.C., Teyssier, C., and Whitney, D.L., 2011, Flow of partially molten crust and the internal dynamics of a migmatite dome, Naxos, Greece: Tectonics, v. 30, p. TC3001, doi:10.1029/2010TC002751.

Kuhlemann, J., Frisch, W., Dunkl, I., Kázmér, M., and Schmiedl, G., 2004, Miocene siliciclastic deposits of Naxos Island: Geodynamic and environmental implications for the evolution of the southern Aegean Sea (Greece), *in* Bernet, M., and Spiegel, C., eds., Detrital Thermochronology—Provenance Analysis, Exhumation, and Landscape Evolution of Mountain Belts: Geological Society of America Special Paper 378, p. 51–65.

Kumerics, C., Ring, U., Brichau, S., Glodny, J., and Monié, P., 2005, The extensional Messaria shear zone and associated brittle detachment faults, Aegean Sea, Greece: Journal of the Geological Society of London, v. 162, p. 701–721, doi:10.1144/0016-764904-041.

Lee, J., and Lister, G.S., 1992, Late Miocene ductile extension and detachment faulting, Mykonos, Greece: Geology, v. 20, p. 121–124, doi:10.1130/0091-7613(1992)020<0121:LMDEAD>2.3.CO;2.

Le Pichon, X., and Angelier, J., 1981, The Aegean Sea: Philosophical Transactions of the Royal Society of London, v. 300, p. 357–372, doi:10.1098/rsta.1981.0069.

Lister, G.S., and Davis, G.A., 1989, The origin of metamorphic core complexes and detachment faults formed during Tertiary continental extension in the northern Colorado River region, U.S.A.: Journal of Structural Geology, v. 11, p. 65–94, doi:10.1016/0191-8141(89)90036-9.

Lister, G.S., Banga, C., and Feenstra, A., 1984, Metamorphic core complexes of Cordilleran type in the Cyclades, Aegean Sea, Greece: Geology, v. 12, p. 221–225, doi:10.1130/0091-7613(1984)12<221:MCCOCT>2.0.CO;2.

Liu, J.L., Tang, Y., Tran, M.-D., Cao, S.Y., Zhao, Z.C., Zhao, Z.D., and Chen, W., 2012, The nature of the Ailao Shan–Red River (ASRR) shear zone: Constraints from structural, microstructural and fabric analyses of metamorphic rocks from the Diancang Shan, Ailao Shan and Day Nui Con Voi massifs: Journal of Asian Earth Sciences, v. 47, p. 231–251, doi:10.1016/j.jseaes.2011.10.020.

Marsellos, A.E., Kidd, W.S.F., and Garver, J.I., 2010, Extension and exhumation of the HP/LT rocks in the Hellenic forearc ridge: American Journal of Science, v. 310, p. 1–36, doi:10.2475/01.2010.01.

Martin, L., Duchêne, S., Deloule, E., and Vanderhaeghe, O., 2006, The isotopic composition of zircon and garnet: A record of the metamorphic history of Naxos, Greece: Lithos, v. 87, p. 174–192, doi:10.1016/j.lithos.2005.06.016.

Martin, L.A.J., Duchêne, S., Deloule, E., and Vanderhaeghe, O., 2008, Mobility of trace elements and oxygen in zircon during metamorphism: Consequences for geochemical tracing: Earth and Planetary Science Letters, v. 267, p. 161–174, doi:10.1016/j.epsl.2007.11.029.

McDougall, I., and Harrison, M.T., 1999, Geochronology and Thermochronology by the ^{40}Ar/^{39}Ar Method (2nd ed.): Oxford, UK, Oxford University Press, 269 p.

Mehl, C., Jolivet, L., Lacombe, O., Labrousse, L., and Rimmele, G., 2007, Structural evolution of Andros (Cyclades, Greece): A key to the behaviour of a (flat) detachment within an extending continental crust, *in* Taymaz, T., Yilmaz, Y., and Dilek, Y., eds., The Geodynamics of the Aegean and Anatolia: Geological Society of London Special Publication 291, p. 41–73, doi:10.1144/SP291.3.

Menant, A., Jolivet, L., Augier, R., and Skarpelis, N., 2013, The North Cycladic detachment system and associated mineralization, Mykonos, Greece: Insights on the evolution of the Aegean domain: Tectonics, v. 32, p. 433–452, doi:10.1002/tect.20037.

Methner, K., Mulch, A., Teyssier, C., Wells, M.L., Cosca, M.A., Gottardi, R., Gébelin, A., and Chamberlain, C.P., 2015, Eocene and Miocene extension, meteoric fluid infiltration, and core complex formation in the Great Basin (Raft River Mountains, Utah): Tectonics, v. 34, p. 680–693, doi:10.1002/2014TC003766.

Michibayashi, K., and Masuda, T., 1993, Shearing during progressive retrogression in granitoids: Abrupt grain size reduction of quartz at the plastic-brittle transition for feldspar: Journal of Structural Geology, v. 15, p. 1421–1432, doi:10.1016/0191-8141(93)90003-S.

Mulch, A., and Cosca, M., 2004, Recrystallization or cooling ages: In situ UV-laser ^{40}Ar/^{39}Ar geochronology of muscovite in mylonitic rocks: Journal of the Geological Society of London, v. 161, p. 573–582, doi:10.1144/0016-764903-110.

Neubauer, F., 2005, Structural control of mineralizations in metamorphic core complexes, *in* Mao, J., and Bierlein, F.P., eds., Mineral Deposit Research: Meeting the Global Challenge: Berlin, Springer, p. 561–564, doi:10.1007/3-540-27946-6_144.

Okrusch, M., and Bröcker, M., 1990, Eclogites associated with high-grade blueschist in the Cyclades archipelago, Greece: A review: European Journal of Mineralogy, v. 2, p. 451–478, doi:10.1127/ejm/2/4/0451.

Parra, T., Vidal, O., and Jolivet, L., 2002, Relation between the intensity of deformation and retrogression in blueschist metapelites of Tinos Island (Greece) evidenced by chlorite-mica local equilibria: Lithos, v. 63, p. 41–66, doi:10.1016/S0024-4937(02)00115-9.

Passchier, C.W., and Trouw, R.A.J., 2005, Microtectonics: Berlin, Springer-Verlag, 366 p.

Pe-Piper, G., Kotopouli, C.N., and Piper, D.J.W., 1997, Granitoid rocks of Naxos, Greece; regional geology and petrology: Geological Journal, v. 32, p. 153–171, doi:10.1002/(SICI)1099-1034(199706)32:2<153::AID-GJ737>3.0.CO;2-1.

Perchuk, L.L., Podlesskii, K.K., and Aranovich, L.Y., 1991, Thermodynamics of some framework silicates and their equilibria: Application to geothermobarometry, *in* Perchuk, L.L., eds., Progress in Metamorphic and Magmatic Petrology: Cambridge, UK, Cambridge University Press, p. 131–164, doi:10.1017/CBO9780511564444.009.

Platt, J.P., Behr, W.M., and Cooper, F.J., 2015, Metamorphic core complexes: Windows into the mechanics and rheology of the crust: Journal of the Geological Society of London, v. 172, p. 9–27, doi:10.1144/jgs2014-036.

Prior, D.J., Trimby, P.W., Weber, U.D., and Dingley, D.J., 1996, Orientation contrast imaging of microstructures in rocks using forescatter detectors in the scanning electron microscope: Mineralogical Magazine, v. 60, p. 859–869, doi:10.1180/minmag.1996.060.403.01.

Reddy, S.M., and Potts, G.J., 1999, Constraining absolute deformation ages: The relationship between deformation mechanisms and isotope systematics: Journal of Structural Geology, v. 21, p. 1255–1265, doi:10.1016/S0191-8141(99)00032-2.

Ridolfi, F., and Renzulli, A., 2012, Calcic amphiboles in calc-alkaline and alkaline magmas: Thermobarometric and chemometric empirical equations valid up to 1,130°C and 2.2 GPa: Contributions to Mineralogy and Petrology, v. 163, p. 877–895, doi:10.1007/s00410-011-0704-6.

Rieser, A.B., Liu, Y., Genser, J., Neubauer, F., Handler, R., Friedl, G., and Ge, X.H., 2006, $^{40}Ar/^{39}Ar$ ages of detrital white mica constrain the Cenozoic development of the intracontinental Qaidam Basin, China: Geological Society of America Bulletin, v. 118, p. 1522–1534.

Ring, U., Laws, S., and Bernet, M., 1999, Structural analysis of a complex nappe sequence and late-orogenic basins from the Aegean Island of Samos: Journal of Structural Geology, v. 21, p. 1575–1601.

Ring, U., Layer, P.W., and Reischmann, T., 2001, Miocene high-pressure metamorphism in the Cyclades and Crete, Aegean Sea, Greece: Evidence for large-magnitude displacement on the Cretan detachment: Geology, v. 29, p. 395–398, doi:10.1130/0091-7613(2001)029<0395:MHPMIT>2.0.CO;2.

Ring, U., Will, T., Glodny, J., Kumerics, C., Gessner, K., Thomson, S., Güngör, T., Monié, P., Okrusch, M., and Drüppel, K., 2007, Early exhumation of high-pressure rocks in extrusion wedges: The Cycladic blueschist unit in the eastern Aegean, Greece and Turkey: Tectonics, v. 26, p. TC2001, doi:10.1029/2005TC001872.

Ring, U., Glodny, J., Will, J., and Thomson, S., 2010, The Hellenic subduction system: High-pressure metamorphism, exhumation, normal faulting, and large-scale extension: Annual Review of Earth and Planetary Sciences, v. 38, p. 45–76, doi:10.1146/annurev.earth.050708.170910.

Royden, L.H., and Papanikolaou, D.J., 2011, Slab segmentation and late Cenozoic disruption of the Hellenic arc: Geochemistry Geophysics Geosystems, v. 12, p. Q03010, doi:10.1029/2010GC003280.

Sanchez-Gomez, M., Avigad, D., and Heimann, A., 2002, Geochronology of clasts in allochthonous Miocene sedimentary sequences on Mykonos and Paros Islands: Implications for back-arc extension in the Aegean Sea: Journal of the Geological Society of London, v. 159, p. 45–60, doi:10.1144/0016-764901031.

Scaillet, S., 2000, Numerical error analysis in $^{40}Ar/^{39}Ar$ dating: Earth and Planetary Science Letters, v. 162, p. 269–298.

Schenk, O., Urai, J.L., and van der Zee, W., 2007, Evolution of boudins under progressively decreasing pore pressure—A case study of pegmatites enclosed in marble deforming at high grade metamorphic conditions, Naxos, Greece: American Journal of Science, v. 307, p. 1009–1033, doi:10.2475/07.2007.03.

Schmid, S.M., and Casey, M., 1986, Complete fabric analysis of some commonly observed quartz *c*-axis patterns, *in* Hobbs, B.E., and Heard, H.C., eds., Mineral and Rock Deformation: Laboratory Studies: American Geophysical Union Geophysical Monograph 36, p. 263–286.

Schmidt, M.W., 1992, Amphibole composition in tonalite as a function of pressure: An experimental calibration of the al-in-hornblende barometer: Contributions to Mineralogy and Petrology, v. 110, p. 304–310, doi:10.1007/BF00310745.

Scott, S., Driesner, T., and Weis, P., 2015, Geologic controls on supercritical geothermal resources above magmatic intrusions: Nature Communications, v. 6, p. 7837, doi:10.1038/ncomms8837.

Seward, D., Vanderhaeghe, O., Siebenaller, L., Thomson, S., Hibsch, C., Zingg, A., Holzner, P., Ring, U., and Duchêne, S., 2009, Cenozoic tectonic evolution of Naxos Island through a multi-faceted approach of fission-track analysis, *in* Ring, U., and Wernicke, B., eds., Extending a Continent: Architecture, Rheology, and Heat Budget: Geological Society of London Special Publication 321, p. 179–196, doi:10.1144/SP321.9.

Shimamoto, T., 1989, The origin of S-C mylonites and a new fault-zone model: Journal of Structural Geology, v. 11, p. 51–64, doi:10.1016/0191-8141(89)90035-7.

Sibson, R.H., 1977, Fault rocks and fault mechanisms: Journal of the Geological Society of London, v. 133, p. 191–213, doi:10.1144/gsjgs.133.3.0191.

Siebenaller, L., Boiron, M.C., Vanderhaeghe, O., Hibsch, C., Jessell, M.W., Andremayer, A.S., France-Lanord, C., and Photlades, A., 2013, Fluid record of rock exhumation across the brittle-ductile transition during formation of a metamorphic core complex (Naxos Island, Cyclades, Greece): Journal of Metamorphic Geology, v. 31, p. 313–338, doi:10.1111/jmg.12023.

Simpson, C., 1985, Deformation of granitic rocks across the brittle-ductile transition: Journal of Structural Geology, v. 7, p. 503–511, doi:10.1016/0191-8141(85)90023-9.

Steiger, R.H., and Jäger, E., 1977, Subcommission on Geochronology: Convention on the use of decay constants in geo- and cosmochronology: Earth and Planetary Science Letters, v. 36, p. 359–362, doi:10.1016/0012-821X(77)90060-7.

Stipp, M., Stünitz, H., Heilbronner, R., and Schmid, S., 2002, The eastern Tonale fault zone: A 'natural laboratory' for crystal plastic deformation of quartz over a temperature range from 250 to 700 °C: Journal of Structural Geology, v. 24, p. 1861–1884, doi:10.1016/S0191-8141(02)00035-4.

Sullivan, W.A., and Beane, R.J., 2010, Asymmetrical quartz crystallographic fabrics produced during constrictional deformation: Journal of Structural Geology, v. 32, p. 1430–1443, doi:10.1016/j.jsg.2010.08.001.

Tirel, C., Brun, J.-P., and Burov, E., 2008. Dynamics and structural development of metamorphic core complexes: Journal of Geophysics Research, v. 113, p. B04403, doi:10.1029/2005JB003694.

Tomaschek, F., Kennedy, A.K., Villa, I.M., Lagos, M., and Ballhaus, C., 2003, Zircons from Syros, Cyclades, Greece—Recrystallization and mobilization of zircon during high-pressure metamorphism: Journal of Petrology, v. 44, p. 1977–2002, doi:10.1093/petrology/egg067.

Tullis, J., and Yund, R.A., 1989, Hydrolytic weakening of quartz aggregates: The effects of water and pressure on recovery: Geophysical Research Letters, v. 16, no. 11, p. 1343–1346, doi:10.1029/GL016i011p01343.

Urai, J.L., and Feenstra, A., 2001, Weakening associated with the diaspore-corundum dehydration reaction in metabauxites; an example from Naxos (Greece): Journal of Structural Geology, v. 23, p. 941–950, doi:10.1016/S0191-8141(00)00165-6.

Urai, J.L., Schuiling, R.D., and Jansen, J.B.H., 1990, Alpine deformation on Naxos (Greece), *in* Knipe, R.J., and Rutter, E.H., eds., Deformation Mechanisms, Rheology and Tectonics: Geological Society of London Special Publication 54, p. 509–522, doi:10.1144/GSL.SP.1990.054.01.47.

Vanderhaeghe, O., 2004, Structural development of the Naxos migmatite dome, *in* Whitney, D.L, Teyssier, C., and Siddoway, C.S., eds., Gneiss Domes in Orogeny: Geological Society of America Special Paper 380, p. 211–227, doi:10.1130/0-8137-2380-9.211.

Vanderhaeghe, O., Hibsch, C., Siebenaller, L., Duchêne, S., de St Blanquat, M., Kruckenberg, S., Fotiadis, A., and Martin, L., 2007, Penrose Conference—Extending a Continent—Naxos Field Guide, *in* Lister, G., Forster, M., and Ring, U., eds., Inside the Aegean Metamorphic Core Complexes: Journal of the Virtual Explorer, v. 27, paper 4, doi:10.3809/jvirtex.2007.00175.

van Hinsbergen, D.J.J., Straathof, G.B., Kuiper, K.F., Cunningham, W.D., and Wijbrans, J., 2008, No vertical axis rotations during Neogene transpressional orogeny in the NE Gobi Altai: Coinciding Mongolian and Eurasian Early Cretaceous apparent polar wander paths: Geophysical Journal International, v. 173, p. 105–126, doi:10.1111/j.1365-246X.2007.03712.x.

Verdel, C., Wernicke, B.P., Ramezani, J., Hassanzadeh, J., Renne, P.R., and Spell, T.L., 2007, Geology and thermochronology of Tertiary Cordilleran-style metamorphic core complexes in the Saghand region of central Iran: Geological Society of America Bulletin, v. 119, p. 961–977, doi:10.1130/B26102.1.

Vermeesch, P., Seward, D., Latkoczy, C., Wipf, M., Günther, D., and Baur, H., 2007, Alpha-emitting mineral inclusions in apatite, their effect on (U-Th)/He ages, and how to reduce it: Geochimica et Cosmochimica Acta, v. 71, p. 1737–1746, doi:10.1016/j.gca.2006.09.020.

Vidal, O., Parra, T., and Trotet, F., 2001, A thermodynamic model for Fe-Mg aluminous chlorite using data from phase equilibrium experiments and natural pelitic assemblages in the 100–600 °C, 1–25 kbar range: American Journal of Science, v. 301, p. 557–592, doi:10.2475/ajs.301.6.557.

Vidal, O., Parra, T., and Vieillard, P., 2005, Experimental data on the Tschermak solid solution in Fe-chlorites: Application to natural examples and possible role of oxidation: The American Mineralogist, v. 90, p. 347–358, doi:10.2138/am.2005.1554.

Whitney, D.L., Teyssier, C., Rey, P., and Buck, R.W., 2013, Continental and oceanic core complexes: Geological Society of America Bulletin, v. 125, p. 273–298, doi:10.1130/B30754.1.

Wijbrans, J.R., and McDougall, I., 1986, $^{40}Ar/^{39}Ar$ dating of white micas from an Alpine high-pressure metamorphic belt on Naxos (Greece): The resetting of the argon isotopic system: Contributions to Mineralogy and Petrology, v. 93, p. 187–194, doi:10.1007/BF00371320.

Wijbrans, J.R., and McDougall, I., 1988, Metamorphic evolution of the Attic Cycladic metamorphic belt on Naxos (Cyclades, Greece) utilizing $^{40}Ar/^{39}Ar$ age spectrum measurements: Journal of Metamorphic Geology, v. 6, p. 571–594, doi:10.1111/j.1525-1314.1988.tb00441.x.

Wijbrans, J.R., Schliestedt, M., and York, D., 1990, Single grain argon laser probe dating of phengites from the blueschist to greenschist transition on Sifnos (Cyclades, Greece): Contributions to Mineralogy and Petrology, v. 104, p. 582–593, doi:10.1007/BF00306666.

Wijbrans, J.R., Pringle, M.S., Koppers, A.A.P., and Schveers, R., 1995, Argon geochronology of small samples using the Vulkaan argon laserprobe: Proceedings of the Koninklijke Academie Wetenschappen, v. 98, p. 185–218.

Xu, H.J., Jin, Z.M., Mason, R., and Ou, X.G., 2009, Magnetic susceptibility of ultrahigh pressure eclogite: The role of retrogression: Tectonophysics, v. 475, p. 279–290, doi:10.1016/j.tecto.2009.03.020.

Yardley, B., Gleeson, S., Bruce, S., and Banks, D., 2000, Origin of retrograde fluids in metamorphic rocks: Journal of Geochemical Exploration, v. 69–70, p. 281–285, doi:10.1016/S0375-6742(00)00132-1.

Zong, K.Q., Liu, Y.S., Hu, Z.C., Kusky, T., Wang, D.B., Gao, C.G., Gao, S., and Wang, J.Q., 2010, Melting-induced fluid flow during exhumation of gneisses of the Sulu ultrahigh-pressure terrane: Lithos, v. 120, p. 490–510, doi:10.1016/j.lithos.2010.09.013.

Science Editor: David I. Schofield
Associate Editor: Enrico Tavarnelli

Manuscript Received 3 February 2016
Revised Manuscript Received 5 May 2016
Manuscript Accepted 30 July 2016

Printed in the USA